Theoretically Predicted Production Cross-Section of Z-boson and a bottom quark in proton-proton collisions.

By

Muhammad Anees Khan

SUBMITTED IN PARTIAL FULFILLMENT OF THE
REQUIREMENT FOR THR DEGREE OF
MASTER OF PHILOSOPHY
AT
DEPARTMENT OF PHYSICS QUAID-I-AZAM
UNIVERSITY,ISLAMABAD

Certificate

The undersigned hereby certify that they have read and recommend to the department of physics for acceptance of thesis entitled **"Theoretically Predicted Production Cross-Section of Z-boson and a bottom quark in proton-proton collisions"** by **Muhammad Anees Khan** in partial fullfillment of the requirements for the degree of **Master of Philosophy**.

Supervisor:
Dr. Shamona Fawad Qazi
Associate Professor
Department of Physics
Quaid-i-Azam University
Islamabad.

Submitted Through:
Dr. Nawazish Ali Khan
Professor
Department of Physics
Quaid-i-Azam University
Islamabad.

Copyright Notice

Author: **Muhammad Anees Khan**
Title: **Theoretically Predicted Production Cross-Section of Z-boson and a bottom quark in proton-proton collisions**
Department: **Physics**
Degree: M.Phil Convocation: year:

Signature of Author

Acknowledgments

I cannot express enough thanks to Dr. Nawazish Ali Khan chairman department of physics, for giving me the opportunity to do research in National Center of Physics and providing invaluable guidance throughout this research.
I would like to express my sincere thanks to Dr. Shamona Fawad Qazi for her assistance through my whole duration of M.Phil. She helped me to put my ideas, well above the level of simplicity and into something concrete. I would like to acknowledge her assistance in reading and correcting this thesis.
I would like to express my special thanks of gratitude to Dr.Wajid Ali Khan who give me the golden opportunity to do this work and also for his patience, kindness and wisdom he has given to me during the whole work. Dr. Wajid Ali Khan is the person who open my mind for the experimental high energy physics. His kind suggestions and words guided me through my whole analysis.
Thanks to all the members in High Energy Physics group at the National Center for Physics (NCP), especially Dr. Muhammad Ahmed , Muhammad Gul for their positive criticism and continuous support and encouragement through the early stages of chaos and confusion. Thanks to Dr. Ashfaq Ahmad, Dr. Irfan Ashgar, Dr. Mohammad Ahmed, Sharjeel Kashif, Sheikh Mansoor who helped me in completing this work.
The greatest thanks goes to my beloved parents who encouraged me when ever I faced difficulties. I am also grateful to my clasmate and a good friend Mr. Muhammad Irfan who also helped me in the whole work. We discuss our problems in computation with each other and he give me his good ides about solutions. Last but not the lest I also thankfull to Google from where I found solution for all my issues related to thesis work.

Muhammad Anees Khan
March 2022.

Abstract

The cross sections of Z-boson and b-quark(jet) is experimentally measured by CMS and ATLAS at the Large Hadron Collider (LHC) in proton-proton collisions at various center of mass energies. Theoretically predicted cross section of the Z-boson and b-quark(jet) production in proton-proton collisions at $\sqrt{s} = 13\ TeV$, $\sqrt{s} = 13.6\ TeV$ and $\sqrt{s} = 14\ TeV$ are presented in this thesis.

The Z-boson and b-quark(jet) production cross section measurement at hadron collision provides a deep understanding of quantum chromodynamics (QCD) and electroweak (EW) processes. The production of Z-bosons and b-quarks(jet) are best examples of hard scattering processes at Large Hadron Collider. Theoretical predictions in perturbative chromodynamics are available at next-to-Leading order (NLO).

Theoretically predicted cross-sections are compared with the measured results at various center of mass energies. Kinematics of b-quarks are also presented.

Measured cross-sections are compared to predictions from the Monte Carlo generator (MADGRAPH5) based on leading-order (LO) or next-to-leading-order (NLO) matrix elements interfaced with pythia parton-shower simulation and evaluating several flavour approaches for the choice of initial-state partons. At NLO accuracy,The 5-flavour number scheme predictions accord better with data than 4-flavour number scheme predictions. In occurrences involving at least one b-quark(jet), the 4-flavour number method underpredicts data.

Contents

List of Figures

List of Tables

Chapter 1

Introduction

"What does matter consist of?" For thousands of years, people have struggled with this dilemma. The components, Wood, fire, earth, metal, and water are all elements that may be found in nature, according to ancient Chinese philosophers, are the five components that make up matter. Since the 17th century, scientists have discovered that everything is made up of atoms which have a size of 10^{-10}m. J.J. Thomson who discovered (e^{-}) electron in 1897 marked the beginning of elementary particle physics. Rutherfrld's renowned scattering experiment in 1909 revealed that the nucleus, with a diameter of 10^{-14}m, lies in the core of the atom. Particle physics is becoming increasingly accomplished with the discovery of the proton, neutron, photon, muon, neutrino, quarks, and gluons.
We know the atom is made up of electrons revolving around a nucleus made out of protons and neutrons which are made up of quarks , thanks to the excellent scientists.

The Standard Model provides a detailed description of these basic particles and interactions."[27, 33, 39, 30]. This chapter will provide a fundamental understanding of Standard Model. It gives a general review of the fundamental particles, their interactions, and their connections.

1.1 Standard Model

At the most fundamental level,The Standard Model is the most thorough explanation of basic particles and interactions available.

Figure 1.1: A comprehensive journey to Quarks.The figure is taken from Reference [28].

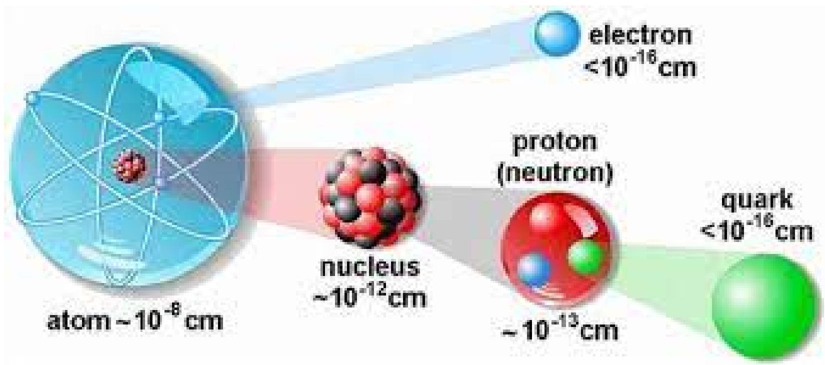

All interation between elementery particles can characterized by four forces

1. Strong Force
2. Gravitational Force
3. Weak Force
4. Electromagnatic Force

The gravitational force is not included in the SM because it may be ignored at the elementary level if the energy is less than the Planck scale 1.22×10^{19}eV. The elementary particles are classified as fermions and bosons according to the SM, depending on whether they have integer or half integer spin, as seen in Figure 1.2.
Six kinds of quarks and leptons with spin $\frac{1}{2}$., make up the fermions that make up matter. They are divided into three generations, with each generation 2^{nd} being a heavier version of the 1^{st}. All particles in the 2^{nd} and 3^{rd} generations, with the exception of ν are unstable .There are also antiparticles with exect same value of masses but opposite charge nature. for both quarks and leptons.

Figure 1.2: An overview to the SM's fundamental particles.The figure is taken from the referance [15].

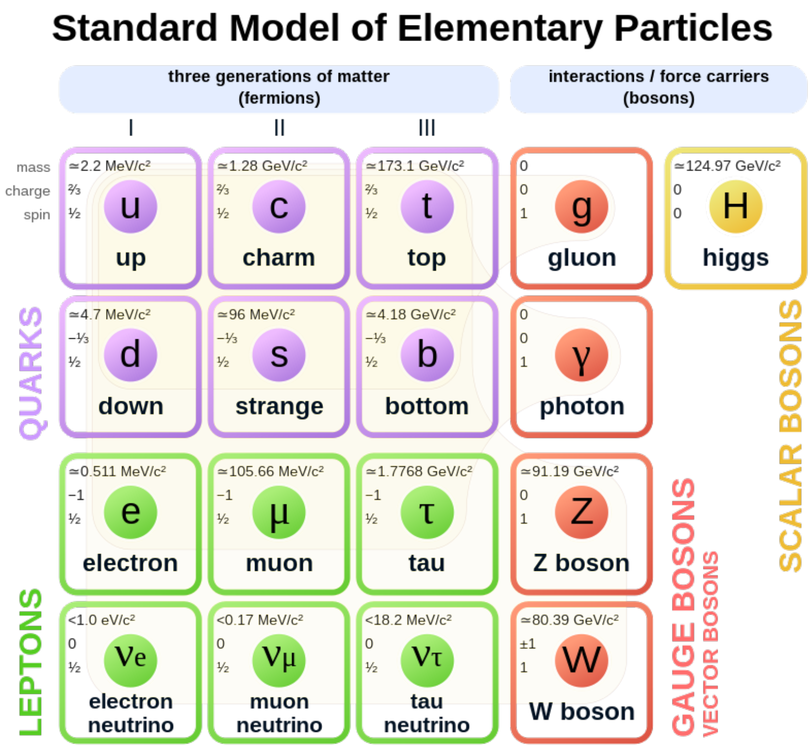

1.1.1 Quarks In Standard Model

As in figure 1.2, Quarks: down (d) , up (u) are in 1^{st} generation; strange (s) and charm (c) are in 2^{nd} generation; top (t) and bottom (b) are in 3^{rd} generation. Each quark has a colour charge and is firmly linked to other quarks to create hadrons, allowing them to interact via strong force. The electric charge of c, u, and t quarks is $\frac{2}{3}$, while the charge of s, b, and d quarks is -$\frac{1}{3}$. Quarks have a weak isospin in addition to the electric charge. As a result, they can interact via electromagnetic and weak force interactions. There have been no single free quarks discovered. *Baryons* are made up of three quarks linked together, like proton and neutron, while *mesons* are made up of a anti-quark and an quark, as pion and kaon. Hadrons are all particles that are formed up of quarks as their constituents.

1.1.2 Leptons In Standard Model

Electron neutrino (ν_e), electron (e) , muon (μ), muon neutrino (ν_μ), tau neutrino (ν_τ), tau (τ) are all leptons. Because the three neutrinos have no eletric charge, They can only interact weakly, making it incredibly difficult to monitor or identify them. The other (τ) , (μ) and (e) have charge of -1, and have the ability to interact both electromagnetically and weakly.

1.1.3 Bosons In standard Model

- **Vector Boson**
  The mediators of the forces in the SM are vector or gauge bosons: (Z, $W^{\pm}$,g ,γ) and scalar boson (H),the Higgs, all with an integer spin. Gluons (g) are responsible for strong interactions , where W^- , W^+ and the Z mediat weak-interections, and the electromagnetic interection the force is carried by the photon (γ). So yet, no gravitational force mediator has been identified. The Table 1.1 lists the four types of forces and some of their features."[27, 33] for more details.

Table 1.1: Illustrations showing the four types of forces, as well as their mediators, ranges, and relative strength.

Interection	Mediators	Range (M)	Relative strength
Strong	glouns	10^{-15}	1
Weak	$W^{\pm}$, Z	10^{-18}	10^{-14}
Electromagnetic	photon (γ)	∞	10^{-3}
Gravitational	gravitons	∞	10^{-43}

- **Scaler Boson**
  "Finally, the Higgs field's quantum manifestation is the scalar boson, the Higgs, which leads to the fermions and also W^+ , W^- and Z bosons getting their masses. The Higgs, discovered in 2012, is a particle with no spin and, electric charge, or colour charge."[27].

1.2 Fundamental Interactions

"The most fundamental forces between elementary particles, which are thought to make up all matter. The basic interactions characterise the behaviour of matter at all sizes, from subatomic to cosmic"[31]. As shown in Figure 1.3.

Figure 1.3: To the cosmic, seen at right in a Hubble Space Telescope picture of the galaxy NGC 6814, shown at left in an artist's rendition of the proton's three-quark composition [31].

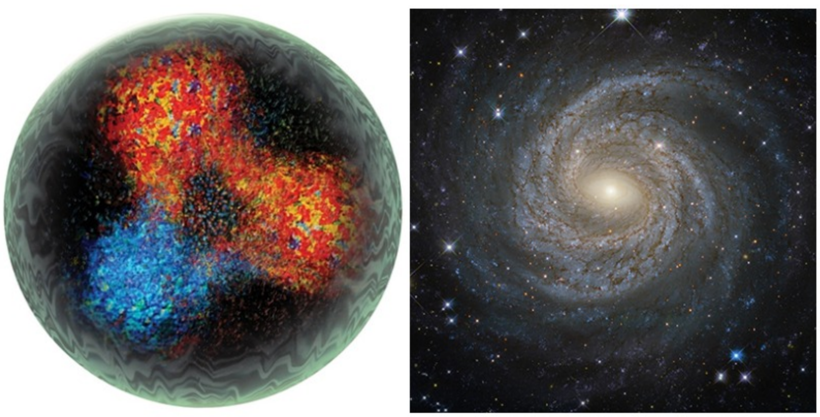

1.2.1 Gravitational Interaction

Gravitational interaction , long-range attraction force that exists between all basic particles. Einstein, a German-born U.S theoretical physicist, proposed general relativity in 1915 , is the greatest description of gravity in terms of quantum mechanics. The force carriers of this force are Known as Gravitons.The graviton's existence, on the other hand, has yet to be proven empirically [31].
The gravitational interaction is substantially weaker than other remaing interactions. No field theory exists till now, for gravitional interaction.

1.2.2 Electromagnetic Interections

These type of interactions can only exist between two charged bodies and are long ranged.

- Attractive for unlike charges.
- Repulsive for like charges.

The electromagnetic force between two charged bodies separated by some distance (r) is given by Equation 1.1.

$$F = \alpha \frac{q_1 q_2}{r^2} \tag{1.1}$$

The α is dimensionless quantity. The value of α determines the strength of electro-magnetic interaction. The other name of α is fine structure constant . α is given by Equation 1.2.

$$\alpha = \frac{1}{137.035999074 \pm 0.000000044} \tag{1.2}$$

Figure 1.4: Feynman diagram of proton-proton electro-magnetic interaction.

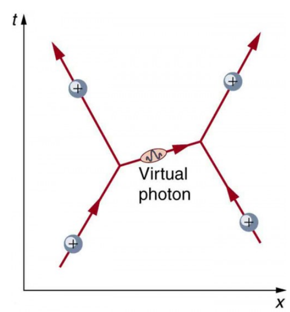

Electromagnetic interaction and forces of attraction or repulsion between charged particles are proved to originate as a result of the basic process of emission of one or more photons in contemporary quantum field theory, as shown in Figure 1.4 .

1.2.3 Weak Interection

The 3^{rd} force or interaction that we are going to discuss in Standard Model is weak force or weak interaction. The neutron's Beta decay is an example of weak interaction as shown below in Figure 1.5 .

n $\xrightarrow{weak}$ $p^{+} + e^{-} + \bar{\nu_e}$

In weak interaction a transformation of particles or flavour occours, same as in the example of neutron's beta decay mentioned above , a neturon is transformed to proton and electron with electron antineutrino. The weak interaction force carriers are W^{+} Z and W^{-} bosons. Mass of Z boson is 91.2GeV/c^2 and mass of W boson is 80.4GeV/c^2.

Figure 1.5: "A free neutron emits a W-, which creates an electron and an antineutrino while it decays. The Figure is taken from Referance [5].

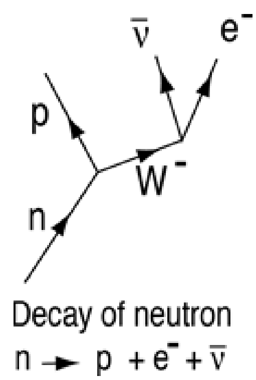

This force is stronger than Gravitational force but it's range is very small which is upto 10^{-18}m.

1.2.4 Strong Interaction

The strong interaction or force is 4^{th} basic force in Standard Model. This is the force which is present between nucleons. A force that can hold nucleons together against the immense forces of proton's repulsion is extremely powerful. This is the force or interaction which is present only between quarks or particles having quark only as their building blocks. By Strong interaction, Protons and neutrons are held together to construct atomic nuclei and it also binds quarks to form hadrons like protons and neutrons as shown in Figure 1.6 .

Although this is the strongest force from all other froces but it

Figure 1.6: Binding of nucleus and nucleons via strong intrection.

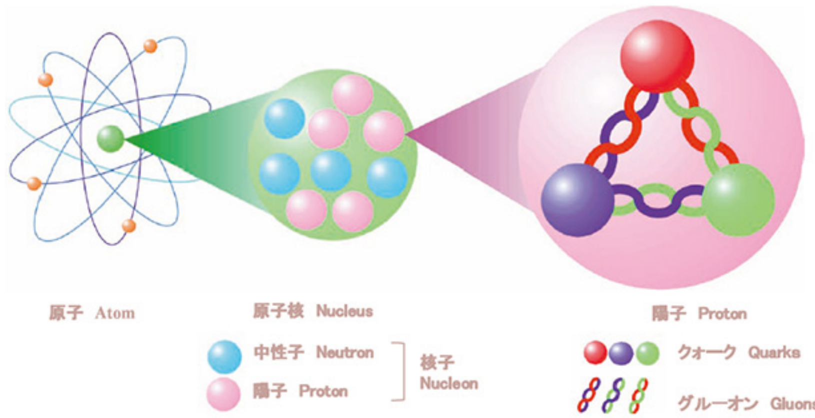

is also a short range force. The effective distance for strong interaction/force is about 10^{-15}m.

The mediator of this force are called gluons. Gluons has zero mass and integer spin.

Because leptons have no quarks, their interaction with each other and with protons and neutrinos lack the strong nuclear force.

1.3 Unification of interactions

Since their discovery and unambiguous categorization, many physicists have tried very hard to combine these four interactions as a single basic interaction between all matter. The work of British physicist and chemist Michael Faraday and Scottish physicist James Clerk Maxwell in the nineteenth century served as a model for such unification ideas, as they merged the distinct forces of electricity and magnetism as part of a single interaction (the gauge interaction of electromagnetism) [31].

1.3.1 Gravitation and electromagnetism

Einstein made the first attempt in this manner when, after understanding gravitation as a manifestation of spacetime curvature, he attempted to explain electromagnetism as another geometrical expression of spacetime features, thereby reaching a unification between both forces. He is said to have failed in this endeavour, to which he committed his final years [31].

1.3.2 Electroweak interaction

The unification of electromagnetic with a weak nuclear interactions is represented by this basic force. The four fundamental forces, strong, electromagnetic, weak , and gravity could only be characterised as separate entities until the early 1970s. Sheldon Lee Glashow of the United States, Abdus Salam of the Pakistan , and Weinberg of United States demonstrated that the electromagnetic and weak nuclear forces may be combined and interpreted as a single interaction called the electroweak interaction. This unification was a great step forward in understanding nature, analogous to the unification of electric and magnetic forces into electromagnetic interactions by Scottish scientist James Clerk Maxwell and colleagues, a century before. The purpose of theoretical physics is to simplify understanding of nature even further by expressing the already known basic interactions in a unified approach [32].
For electroweak unification theory, they shared the 1979 Nobel Prize in Physics.

1.3.3 Grand Unification

The strong force and the electroweak interaction are brought together in grand unified theories (GUTs). M-theory, superstring theory, or a "theory of everything" are terminology for a number of frameworks that attempt to bring gravity, the fourth fundamental interaction, even closer together. According to scientists, all forces were initially linked at the great energy and temperature .The energy and temprature when the cosmos was born at the big bang . The forces began to split as the temperature decreased [32]. The unification of all the forces is shown in Figure 1.7.

Figure 1.7: A graph illustrating the separation of basic interactions as the universe's temperature dropped in instant of a second following the big bang. The electromagnetic and weak interactions, which were formerly unifiable as electroweak interactions, were the last to split.

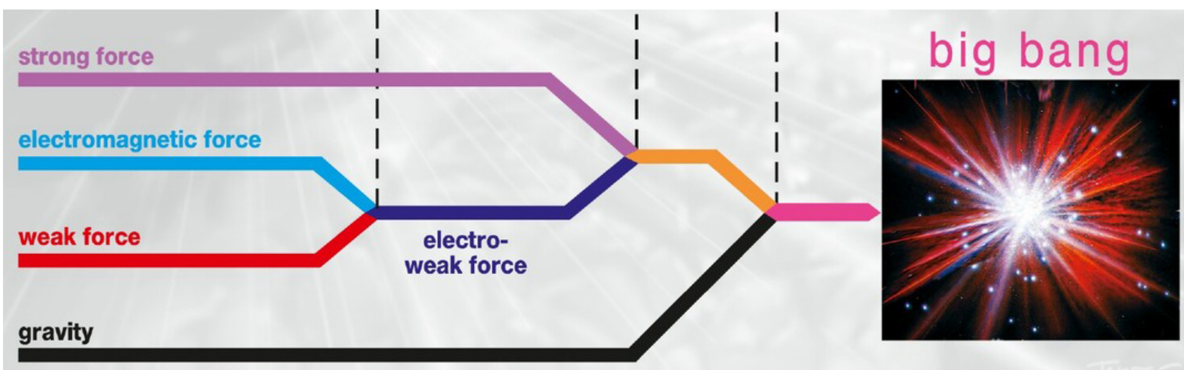

1.4 Higgs mechanism

Electroweak theory alone cannot explain the mechanism by which a W or Z boson acquires mass. Because weak bosons gain mass while γ does not, there must be another force at low energy that breaks this symmetry, and hence at least another virtual particle that conveys this force. The Higgs boson is this virtual particle, and the entire process is known as the Higgs Mechanism [23].
Remember that mass is the manifestation of inertia to understand how particles obtain mass. As the cosmos cools, the higgs field pervades all of space, acting as a pull on every particle that passes through it. The drag of a particle is determined by how efficiently it interacts with the field off Higgs . This drag is equivalent to inertia, and so a plausible mass of previously massless particles appears. All of this happens as a result of a phenomenon known as Spontaneous Symmetry Breakdown [23]
When a system following global symmetrical rules becomes locally asymmetric in its lowest energy state, this is known as spontaneous symmetry breakdown. An example of this is a ball placed in a bowl, that rises in the centre until it must fall one way or the other

Figure 1.8: Illustration of symmetry breakdown.

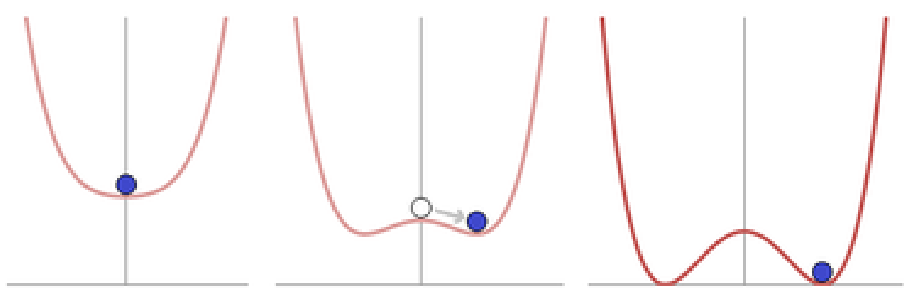

1.5 Limitations of Standard Model

Despite being the most successful particle physics theory to date, the Standard Model is not without flaws. Standard-Model not explain properly some fundamental physical phenomena [11].
What is the flaw in the Standard Model? Essentially, the entire model lacks resilience at greater energy levels. Things behave ap-

propriately as long as we see numerous occurrences at low energy, as we have observed so far. However, as accelerators get more powerful, we are reaching a level of energy similar to that which occurred right after the Big Bang, making the Standard Model calculations shaky. At low and high speeds, this is analogous to the physics principles. Newton's fundamental laws of mechanics are incapable of describing a particle travelling at almost the speed of light. Special relativity is necessary to characterise its motion [35]. Some major problems that standard model is unable to difine are as below

- Gravity
- Neutrino masses
- Dark energy
- Dark matter
- Matter-Antimatter asymmetery

Chapter 2

The hunt for experimental proofs of the Standard Model resulted in the development of technological and experimental settings. New energy regimes had to be investigated when precision experiments were done, providing more tight limits on the SM parameters. To meet this need, the LHC (Large Hadron Collider) was assembled. An accelerator system, LHC (large hadron collider) is a proton-proton collider at CERN that was launched in 2008 as the newest addition to CERN's research facilities . The first half of this chapter will summarise accelerator features, while the second portion will focus on the ATLAS and CMS experiments description.

2.1 The Large Hadron Collider (LHC)

The LHC [16], is the most powerful and biggest particle accelerator in the world. It was constructed in Geneva,at border between Switzerland and France, durring 1998 and 2008. It was placed in the same giant underground tube (Large Electron-Positron Collider) that housed the 26.7km ring a . On average, the Large Electron-Positron Collider (LEP) is 100 metres deep.

Because LHC is a hadronic collider, it can achieve greater energies in the centre of mass frame than LEP due to lower energy losses as a result of synchrotron radiation. It can accelerate two proton beams cycling in opposing directions at a centre of mass energy of 14 TeV (currently 13 TeV), it can also accelerate heavy ion (lead) beams at a centre of mass energy of 5.5 TeV.

In a regime of super high vacuum (10^{-7} Pa), the beams flow in two separate pipelines. They are bent by NbTi superconducting magnets that create a magnetic field of more than 8 T and are chilled to a temperature of -271.3 C with superfluid helium. There are four collision locations along the LHC ring, where the relevant experiments are present. (see Figure 2.1)

1. ALICE (A Large Ion Collider Experiment) [17]
2. ATLAS (A Toroidal LHC ApparatuS) [18]
3. LHCb (Large Hadron Collider beauty) [19]
4. CMS (Compact Muon Solenoid) [34]

Figure 2.1: The four primary LHC experiments are housed in the CERN accelerator.

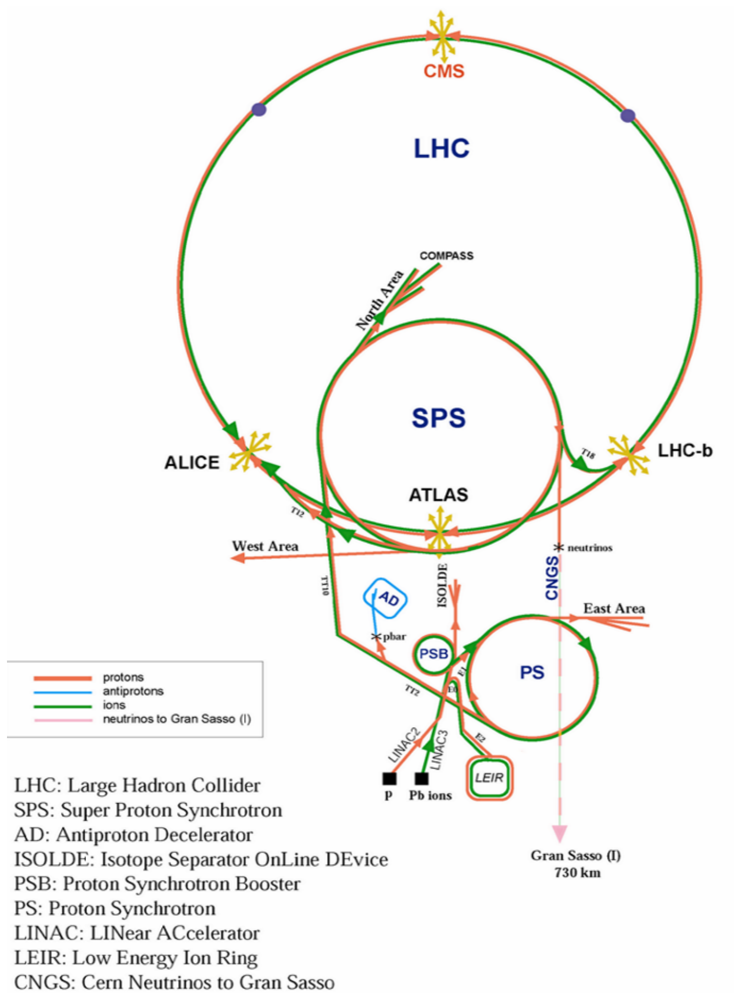

- ATLAS and CMS were created with the goal of studying as many events as possible in proton-proton collisions. They are both multipurpose detectors designed to look at Standard Model physics (finding the Higgs boson) as well as to learn about newer physics that isn't covered by the Standard Model (SUSY in particular).

- ALICE investigates the strong interactions between heavy ions in the presence of a high energy density (when matter is in a plasma state of quarks and gluons). Collisions with lighter ions and at lower energies are also part of the physics programme, as is the collecting of data from proton-proton collisions to serve as standards for the heavy-ion programme.

- The LHCb was constructed to study heavy flavour physics, specifically to look for novel sources of CP violation in hadrons containing bottom and charm quarks beyond the SM.

- The LHCf detector is next to the ATLAS detector, and its objective is to learn more about cosmic rays. It simulates cosmic rays in laboratory circumstances by using particles formed through collisions.

- MoEDAL is the most recent experimental setup (near LHCb) that is used to look for magnetic monopoles.

2.1.1 Accelerator structure

As shown in Figure 2.1 , separate steps of proton beam acceleration are carried out. The protons are created by removing electrons from the hydrogen gas source, extracting them at 91 keV, and injecting them into the LINAC2. This is a 36-meter-long linear accelerator that uses RF(radio-frequency) quadrupoles and focusing quadrupole magnets.The accelerator accelerates protons to energies of 50 MeV. RF cavities are used to break protons into 25ns separate bunches (equivalent to a 40 MHz of frequency) during acceleration. There are approximately 1.1×10^{11} particles in each bunch. The

beam is then directed to the PSB (Proton Synchrotron Booster) , a 157-meter-long round accelerator that boosts the beam energy approximately upto 1.4 GeV. The protons then go to the Proton Synchrotron (PS), a 628-meter ring that boosts their energy to 25 GeV. The Super Proton Synchrotron (SPS, a 6.9 km circumference synchrotron) speedsup the beam even more to 450 GeV before entering the LHC ring. Inside the LHC, eight radio frequency cavities accelerate both proton beams to their current energy of 6.5 TeV in the last step of acceleration.
IThere are 1232 superconducting magnetic dipoles (Figure 2.2) that confine particles into a circular orbit, providing an 8.36 T magnetic field transverse to the beam direction. As previously indicated, the dipoles are chilled to 1.9 K using a cryogenic system that uses superfluid 3 He. The produced field is optimised to limit both beams, which are accelerated concurrently in two separate but close pipes. The beams are further concentrated and collimated around the collision locations, where the experiments are placed, by a system of quadrupolar, sextupolar, and octupolar magnets.
For a given process, the number of events generated per second (N_e) at the LHC is given by Equation 2.1

$$N_e = L\sigma_e \tag{2.1}$$

where L is integrated luminosity , and σ_e is the cross section for the process. The instantaneous luminosty (number of collisions per unit of time and transverse section of the beams) is solely determined by the beam parameters as shown in Equation 2.2

$$L = \frac{N_b^2 n_b f_r \gamma}{4\pi \xi_n \beta^*} F \tag{2.2}$$

where n_b is the number of bunches per beam,γ the relativistic factor, f_r is the revolution frequency, N_b is the number of particles per bunch, ξ_n is the normalised transverse beam emittance, which describes the proton's phase space dispersion , β^* is the beta (β) function at the site of collision , which describes the oscillation of the bunches around the ideal orbit, and the geometric luminosity decrease factor F, due to the crossing angle at the site of interaction.

The integrate luminosity, which is dependent on the instantaneous brightness and the collection time, determines the overall number of interactions in a data acquisition.

During the 13 TeV collisions period (2015-2018, also known as Run II), ATLAS acquired $139 fb^{-1}$ total integrated luminosity. (see Figure 2.3).

Figure 2.2: One of the magnetic dipoles used to bend and stabilise the orbit of the beam [16]

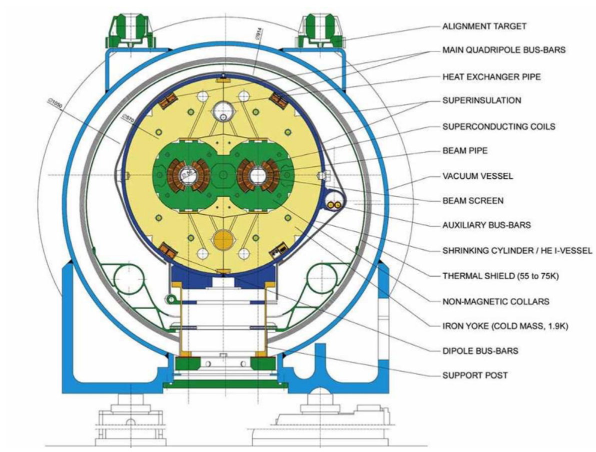

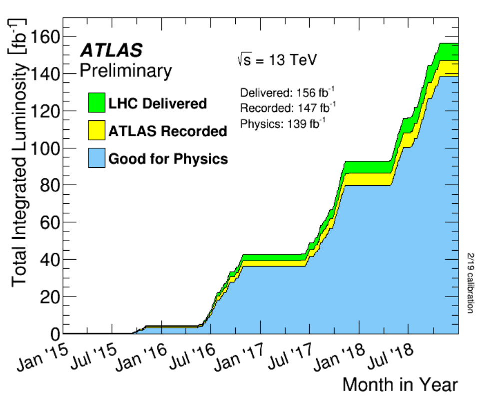

Figure 2.3: Luminosity transmitted to ATLAS (green), recorded (yellow), and validated as excellent quality data (blue) during 13 TeV collisions from 2015 to 2018.[29]

2.1.2 Coordinate system

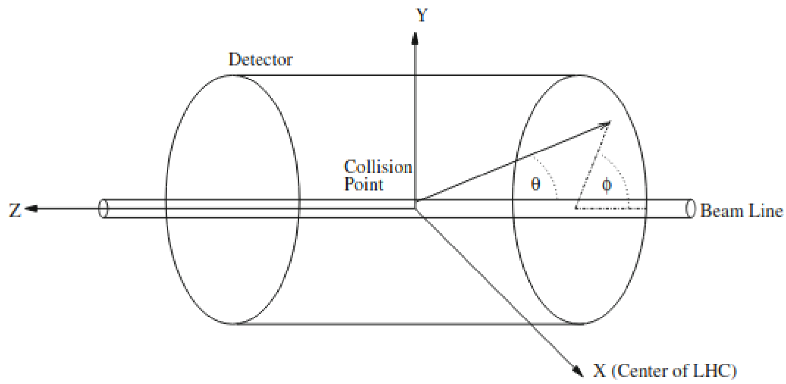

Figure 2.4: ATLAS and CMS coordinate system, Figure taken from referance [26]

ATLAS, like the LHC in general,has right-handed Cartesian coordinate system.The nominal interaction point is at the origin of a right-handed Cartesian coordinate system .
The x-axis is perpendicular to the beam at the origin, with the positive direction pointing to the LHC's centre. The y-axis is also perpendicular to the beam and points upwards. The plane is formed by these two perpendicular axes is called the transverse plane.
Finally, the z-axis is perpendicular (transverse) to the direction of the beam as shown in Figure 2.4.

The ATLAS detector's cylindrical structure recommends that various parameters relevant for properly defining the event should be introduced. These parameters are mentioned below

- $\phi = \cot(\frac{x}{y})$, is the angle around z-axis , azimuthal angle.
- $\theta = \arctan$ $(\frac{y}{z})$, is polar angle measured from z-axis.
- y $= \frac{1}{2}\ln(\frac{E+p_z}{E-p_z})$, is the rapidity of the particle, where E is its energy and p_z is the component of its momentum projected along the beam axis.
- In the case of extremely relativistic particles (m « p), the pseudorapidity η can be used to approximate the rapidity where η = - ln (Tan $(\frac{\theta}{2})$) , un-der Lorentz boosts in the axis direction.

It is a quantity that remains invariant.The value of pseudorapidity is zero at $\theta = \frac{\pi}{2}$,as it gets closer to the beam pipe, it tends to infinity for $\theta = 0$, as shown in Figure 2.5.

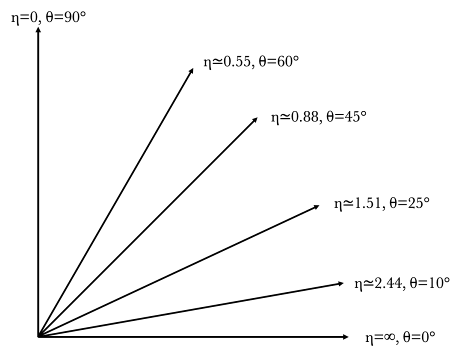

Figure 2.5: pesudorapidity value with respect to θ.

- $\Delta \mathrm{R} = \sqrt{\Delta\eta^2 + \Delta\phi^2}$, is distance in between ϕ - η space.
- $p_t = p\mathrm{Sin}(\theta)$, transverse momentum.
- $E_t = E\mathrm{Sin}(\theta)$, transverse energy.

2.2 Detector Requirments

The LHC's innovative physics mission necessitated the development of new and advanced detectors capable of probing proton-proton and ion-ion collisions. To meet the need, ATLAS and CMS 2 major detectors, were created, with two separate projects probing the Standard Model and Beyond physics. These detectors would have to meet some general standards in order to achieve their objectives ;

- fast and radiation-hard components and electronics.
- To accommodate particle fluxes and decrease the impact of intertwining events, required detectors with very high granularity.
- Need to have good econstruction efficiency and good charged-particle momentum resolution.

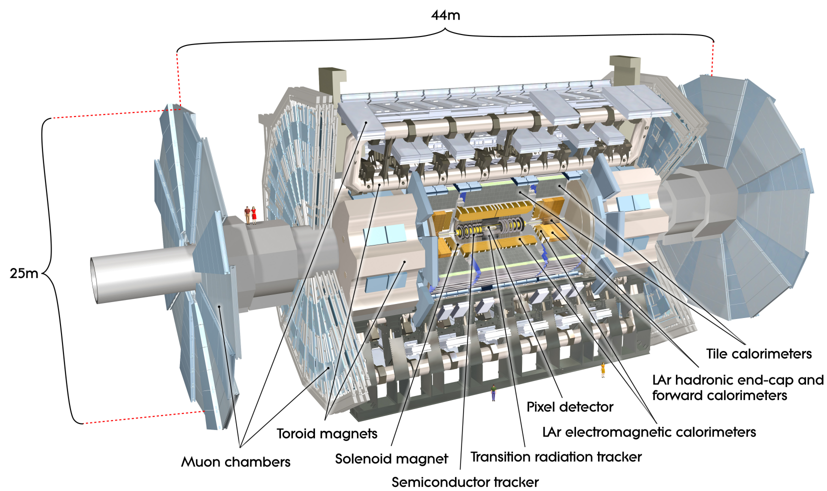

Figure 2.6: A digital picture of the ATLAS, with sub-detectors. Figure is taken from referance [26].

- In terms of pseudorapidity and angular coverage, there is a lot of acceptance needed.
- Electromagnetic calorimeter with excellent electron and photon recognition and measurement capabilities.
- A very good hadronic calorimeter, available for jets and missing transverse energy measurements.
- Good muon measurements , identification
- To achieve a suitable trigger rate for the majority of physics phenomena of interest ,It is necessary to have incredibly accurate triggering on lower transverse-momentum particles with strong background rejections.

2.2.1 The ATLAS Detector

Figure 2.6 shows a view of the largest detector's of LHC, ATLAS. The detector has a height of 25 metres and a length of 44 metres.The detector's total weight is estimated to be over 7000 tonnes. It features a cylindrical form with a barrel in the centre. A thin superconducting solenoid surrounds the inner-detector cavity, and

three huge superconducting toroids enclose the calorimeters (two end-caps, one barrel) .
The structure of ATLAS, like that of many other detectors, is divided into layers of subsystems, each with its own objective as shown in Figure 2.7.

- The Inner Detector (ID) is the component very close to contact site, and it reconstructs the charged particle's track. The ID monitors the charge and momentum of such particles since a 2T magnetic field surrounds it.
- ECAL an Electromagnetic Calorimeter surrounds the ID , these are devices that monitor the energy of photons and electrons.
- The ECAL is encased in the Hadronic Calorimeter (HCAL), which is used to detect the energy of hadronic particles.
- The (MS) Muon Spectrometer is a device that reconstructs the momentum, charge, and route of muons by embedding it in a toroidal magnetic field.

Three smaller detectors are positioned in the forward sections, in addition to this layer structure, to estimate the luminosity provided to ATLAS. To read information from over 100 million electrical channels at a rate of around 40 MHz and preserve physics events at a frequency of about 1 kHz , a three-level Trigger and Data Acquisition (TDAQ) system is used. Table 2.1 summarises the overall performance objectives.

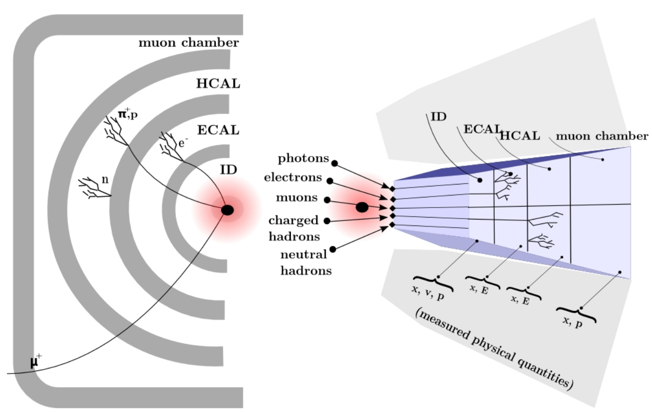

Figure 2.7: A general high energy physics detector is depicted schematically.

Table 2.1: Atlas general performence goals[18]

Detector component	Required resolution	η converge	
		measurment	Trigger
tracking	σ_{p_t} / p_t = 0.05% p_T + 1%	±2.5	
EM calorimetry	σ_E / E = 10% / $\sqrt{E}$ + 0.7%	±3.2	±2.5
Hadronic calorimeter (jets)			
Barrel and end-cap	σ_E / E = 50% / $\sqrt{E}$ + 3%	±3.2	±3.2
forward	σ_E / E = 100% / $\sqrt{E}$ + 3.1%	$3.1 < \|\eta\| < 4.9$	$3.1 < \|\eta\| < 4.9$
Moun spectrometer	$\sigma_{P_T}/p_T = 10\% at p_T = 1TeV$	±2.7	±2.4

2.3 CMS Detector

The Compact Muon Solenoid (CMS) is cylindrical shaped detector, measuring 21.5 metres in length and has 7.4 metres radius. It was built around a superconducting solenoid with a magnetic field of 3.8T. Figure 2.8 depicts a general overview of the detector.

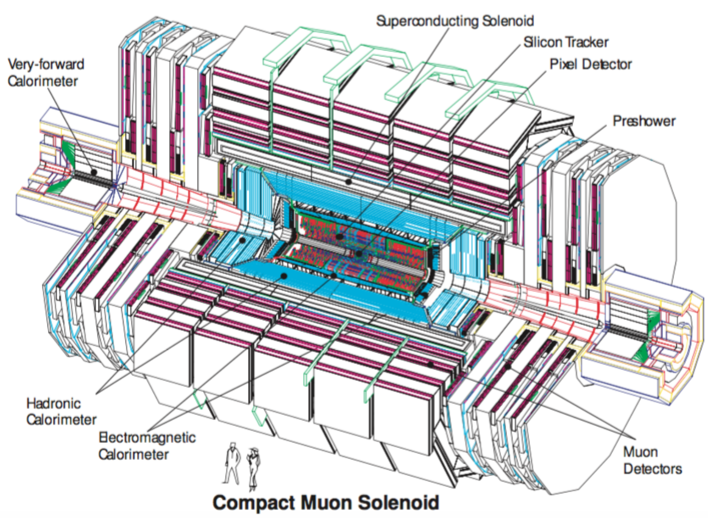

Figure 2.8: CMS detector's overview. Figure from [6].

2.3.1 Overview of CMS detector

The CMS detector features a 21.6 meters long cylinder with a 15 meters of diameter and have 12500 tonnes of weight. It is planned to operate at a 14 TeV center-of-mass energy with $10^{34} cm^{-2} s^{-1}$ of luminosity. All of the inner detectors are surrounded by a superconducting solenoid magnet in the CMS. CMS has a variety of silicon trackers, including pixel and strip trackers, as well as a lead-tungstate ($PbWO_4$) Electromagnetic Calorimeter and a brass scintillator sampling Hadronic Calorimeter. A superconducting solenoid and a muon detector are held together by an iron yoke.
Because CMS has cylindrical symmetry, it's easier to work with cylindrical coordinates (r, θ, ϕ) as shown in Figure 2.10. The CMS

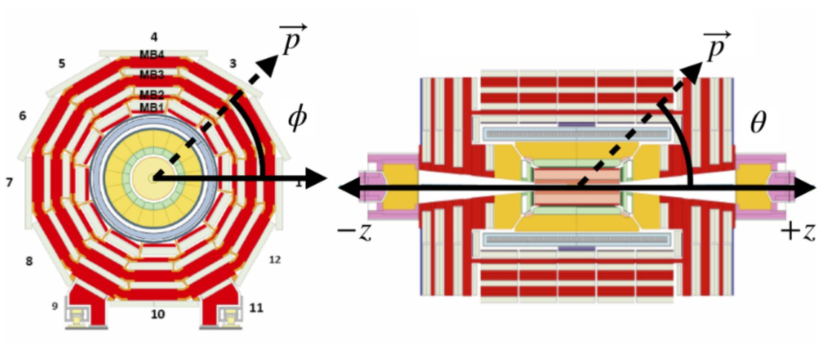

Figure 2.9: CMS polar coordinates. Figure is taken from referance [20].

structure can be summarized as below:

- At the center of the apparatus, interactions between particles take place, with a maximum instantaneous luminosity of $21 nb^{-1} s^{-1}$ reached in LHC RUN 2.
- The silicon Traker is the inner part of detector having radius of $|r| < 1.2m$ from point of interaction with $|\eta|$ in the range of less than 2.5 .
- The Electromagnetic calorimeter (ECAL) is present next to sillicon tracker which is extends to $1.8m > r > 1.2m$ covering $|\eta| < 1.3$ of pseudo rapidity range.
- The Hadronic Calorimeter (HCAL) is the 3^{rd} outer part, which

is extended to the radius of $r < 2.9m$ and covers pseudo rapidity range $|\eta| < 5$.

- The superconducting solenoid magnet provides a magnetic field of 4T along the beam direction, which bends the charged particles trajectories in order to measure their momentum. The solenoid surrounds all the inner detectors and extends from $2.9m < r < 3.8m$ over $|\eta| < 1.5$.
- The muon system is the detector's outermost component. It covers $|\eta| < 2.4$ and extended from $4m < r < 7.4m$.

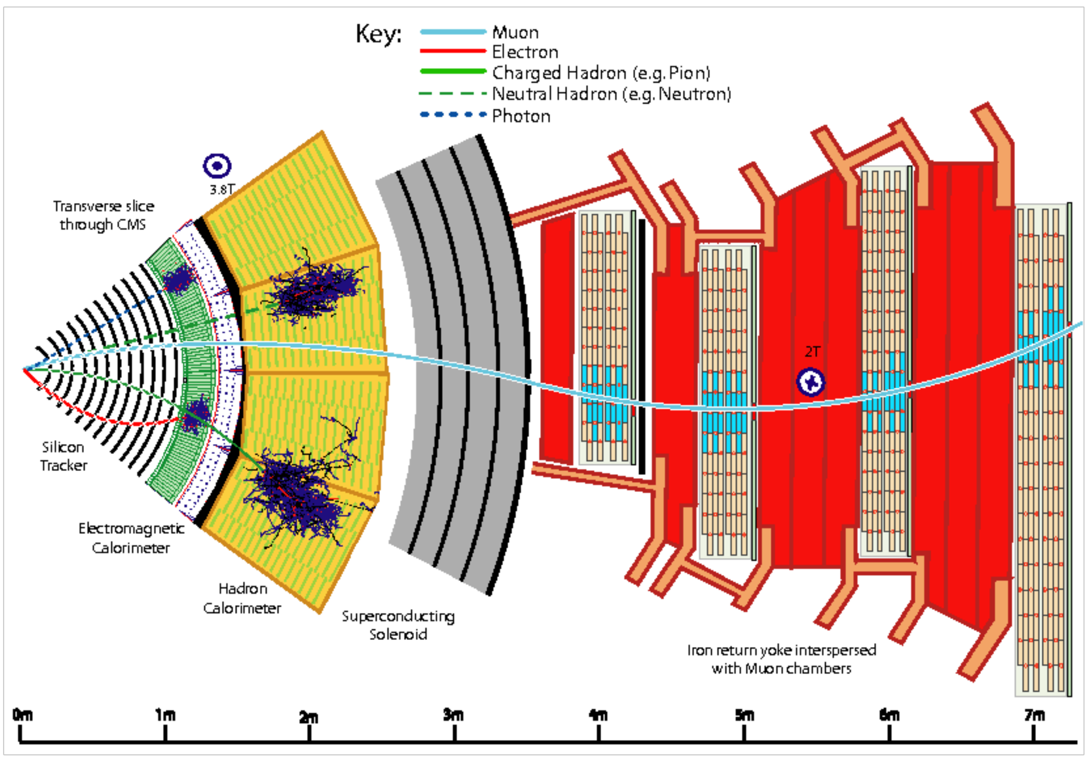

Figure 2.10: CMS Structure. The Figure is taken from referance [10].

Chapter 3

3.1 b-Quark discovery

"*It is the year 1977. The Standard Model is currently in its early stages of development. The existence of protons and neutrons may be explained by a basic two-quark model comprised of up and down quarks. (A proton consists of two up and one down quark, whereas a neutron consists of one up quark and two downs). More evidence of particles made up of quark-antiquark pairs, termed mesons, has emerged, including two new quarks: the charm and the strange. The charm was found as a component of the J/psi meson just recently. Columbia University's Leon Lederman is leading a team at Fermilab working on a detector to identify a new meson called the upsilon*".
At Fermilab, the upsilon was discovered to have a mass of 9.5 GeV, which is 10 times that of the proton.
It's fascinating how the upsilon was discovered. Because of its short duration, this meson is difficult to detect. Dr. Lederman and his colleagues fired a beam of protons at a target. Mesons of many types were created which subsequently decayed. In actuality, the upsilon decomposed into two muons. It was possible to detect and track these muons. The muon's energies and momenta could then be tracked back to locate the new upsilon particle and its mass using the tracking information.
The upsilon's properties have been confirmed as being made up of a new type of quark. This quark was formerly known as "beauty" or "b" but is now more frequently known as the bottom quark and upsilicon is a bound state of quark-anitquark pair.
A b-qark mass is 4.5 times that of a single proton. This is the first of the third generation of quarks. Because each generation has two

sorts of quarks, finding the bottom triggers the hunt for the other one.

3.2 Z Boson

The UA1 collaboration of the $Sp\bar{p}S$ collider at CERN found the Z boson in 1983 [36]. The major objective was to find the massive electroweak interaction intermediate bosons. Eight events were detected by the UA2 detector, which were interpreted in terms of the reaction
$p\ \bar{p} \rightarrow Z +$ anything, with $Z \rightarrow e^{+} + e^{-}$

in a data sample having a total integrated luminosity of $131 nb^{-1}$. Figure 3.1 based on the energy in the clusters of the electromag-

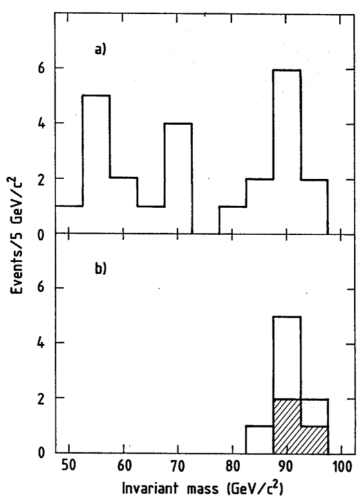

Figure 3.1: At the UA1 experiment, invariant mass distribution of electron pairs as detected for the first Z candidate events given in Figure (a). It depicts the distribution of 24 events that met the energy deposit criterion in electromagnetic clusters. The number of events was further decreased to eight once identification criteria were included, with an invariant mass distribution peaking at a 90 GeV as presented in Figure (b). The shaded band depicts the three instances that surpassed the requirement for an isolated track that matched both electromagnetic clusters.

netic calorimeter, illustrates the distribution of 24 events passing loose criteria. The number of events was decreased to eight and

their distribution as a function of the invariant mass of the dilepton pair, which required at least one isolated charged track with $p_T > 7$GeV pointing to the electromagnetic cluster is shown. The eight events were spread around a mass value of 90 GeV, as seen in the Figure 3.1. Only three occurrences survived (shaded band in following Figure 3.1) the requirment that the single electron's trajectory had to point to both energy deposits in the electromagnetic calorimeter. Following these events, the UA2 collaboration calculated the Z boson's mass to be:
$M_z = (91.9 \pm 1.3 \pm 1.4)$GeV

3.3 Proton-proton interactions at LHC

Calculating the cross section of physics processes at hadron colliders like LHC is challenging due to the delicate interplay between perturbative theoretical calculations, phenomenological models, and the utilisation of experimental data. In order to calculate the process at LHC, the interacting protons must be treated as a composite of quarks and gluons (partons). As a result, the cross section for a process resulting from the interaction of two partons with momenta p_1 and p_2 may be written as given in Equation 3.1.

$$\sigma(p_1, p_2) = \sum_{i,j=q,\bar{q},g} \int_0^1 dx_1 dx_2 f_i(x_1, \mu_f^2, \mu_r^2) f_j(x_2, \mu_f^2, \mu_r^2) \hat{\sigma_{ij}}(x_1 p_1, x_2 p_2, \alpha_s(\mu_R^2), (\frac{Q^2}{\mu_r^2}, \frac{Q^2}{\mu_f^2}) \tag{3.1}$$

The momentum fractions carried by parton 1 and 2 are x_1 and x_2, respectively. The Parton Distribution Fuction (PDF) $f_i(x_1, \mu_f^2, \mu_r^2)$ and $f_j(x_2, \mu_f^2, \mu_r^2)$ represent the likelihood that the parton $i(j)$ will carry a fraction x of the proton 1(2) momentum having re-normalization scale μ_r and factorization scale μ_f [9]. PDFs are dependent on the QCD factorisation scale μ_f , renormalization scale μ_r and are particular to the type of interacting partons. The interaction cross section between the two partons engaged in the interaction is given by σ_{ij}. It is determined by the strong coupling constant (α_s) and the transferred momentum Q^2 for a certain energy scale (the renormalisation scale μ_R). The total is calculated using all contributing parton configurations , all conceivable combinations of quarks, antiquarks, and gluons are represented by 'i" and "j".

The number of observed events N (X) for a particular process ($pp \to X$) with a specified detection efficiency ϵ is determined experimentally by the product of production cross section and where $\int ldt$ is theintegrated luminosity.

$$N(X) = \epsilon.\sigma(X) \int ldt \tag{3.2}$$

3.3.1 The running coupling constant

Understanding the sector of SM that accounts for the strong interaction, Quantum Chromodynamics (QCD) , is particularly important since the current generation of high-energy experiments involves colliding beams of protons (or anti-protons). Strongly interacting particles, such as protons, are defined in terms of their component quarks and gluons in this theory. While this theory will never be totally solved, perturbative expansions can be utilised to make approximate predictions. For each successive term, the expansion is inhibited by one power of α_s. In a number of calculations, the simplest predictions from the first, or lowest order, term in this series have been employed. Because the strong coupling is so massive (much bigger than the similar electromagnetic coupling of 1/137), such calculations have only a limited precision.

In order to establish credible theoretical results to compare with experimental data, it is preferable to compute higher order terms in the perturbative series. These calculations not only give more accurate cross section and event rate estimations, but they also provide more accurate cross section and event rate projections. They're also becoming better at simulating the substructure of colliding hadrons and particle jet formation in detectors.

The cross section evaluation in a perturbative field theory can be defined in terms of the coupling constant while using Feynman diagrams. These diagrams may have particle loops, resulting in computation of divergences. The renormalisability condition of quantum field theory is met by QCD and QED, which permits divergences to be absorbed into renormalized formulations of coupling constants and particle masses [37]. The introduction of an arbitrary scale, the renormalisation scale (μ_R), is the result of this method. As a result, the coupling constant (α_s) fluctuates as a function of μ_R, describing the running behaviour. The running coupling constant (α) can be described by the following general Equation [4]:

$$\alpha(Q^2) = \frac{\alpha(\mu^2)}{1 + \alpha(\mu^2) b_0 ln(\frac{Q^2}{\mu^2})} \tag{3.3}$$

In QCD $b_0 = (33 - 2n_f)/12\pi)$,and in QED $b_0 = -1/3\pi)$, where n_f is quark flavour number. As a function of the energy involved in the process μ^2 and the transmitted momentum Q^2, the sign of b_0 dictates the direction of the running behaviour (i.e. increase or decrease). The total of the four vectors of the interacting parton gives Q^2. In case of Leading-order (LO) resonant scattering $q\bar{q} \to Z$, the energy scale is $Q^2 = sx_1x_2 = M_Z^2$, where s denotes the collision's centre of mass energy. coupling constant as a function of the energy determined by various tests is shown in Figure 3.2.

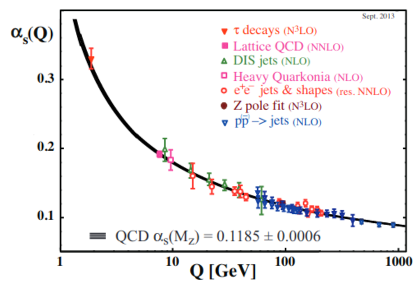

Figure 3.2: The change in the vale of α_s with the energy scale Q and the current world average value is illustrated, Figure taken from reference [8].

3.3.2 Parton Distribution Functions

Richard Feynman coined the term "parton" in 1969 to describe any particle constituent within the proton, neutron, and other hadrons. Quarks and gluons are the modern names for these particles. The three-quark theory, in which a proton or neutron is comprised of three non-interacting free quarks inside a bag, is extremely simplified. Along with the valance quarks, there are many quarks and anti quarks inside hadrons due to the presence of gluons. These all are also called partons. Deep Inelastic Scattering (DIS) of electrons (leptons) from nucleons, during which the lepton acts as a probe, transmitting a four-momentum modulus $|q|$ to the nucleon in the collision, is the greatest way to learn about a nucleon's partonic

structure. In 1996 at SLAC,DIS experiment of electron-proton was the first one to show that the nucleon had a partonic structure.
The probe's resolving power in DIS is roughly $\hbar/|q|$. As a result, the degree of structure displayed rises as $|q|$ rises. The resolution is approximately 0.002fm for $|q|$=100GeV, adequate enough to investigate the nucleon's internal structure. It is easier to think about the nucleon in a frame with a lot of momentum. The momentum of the parton in such a frame is nearly collinear with the momentum of the nucleon , thus it appears as a stream of partons. Each one carries x fraction of the total momentum of proton. Parton Distribution Functions (**PDF**) are the momentum distribution functions of the partons within the proton.At an energy scale $Q^2 = -q^2$, they reflect the probability of parton having x fraction of momentum of proton. The three valence quarks become increasingly prominent in the nucleon as Q^2 decreases or at low energies. There are an increasing number of quark-antiquark pairs having a low momentum fraction x at high Q^2 . They make quarks sea. The DIS discovered that quarks and antiquarks barely carry about half of the nucleon's momentum, leaving the gluons to carry the rest. With rising Q^2, the proportion transported by gluons rises. When the energy Q^2 scale fluctuates, QCD yields quantitative predictions regarding the changing rate of parton distributions. In the perturbative QCD (pQCD) domain, the DGLAP QCD evolution equation governs these predictions.That is, in the case when the $\alpha_s(Q^2)$ of QCD is much less than 1. The equations (DGLAP) have been constructed at many levels of approximation, in relation to different powers of $\alpha_s(Q^2)$ in pQCD development, evolution, and are often referred to as first order i.e. Leading-Order (LO) in $\alpha_s(Q^2)$ or NLO as next to leading order or NNLO as next to next to leading order. Parton Distributions Functions (PDFs) are derived using DGLAP equations. The PDFs are crucial in cross section computation.

$$\sigma(x, Q^2) \approx \sum_a C_a \otimes f(1/A)(x, Q^2) + remainder \tag{3.4}$$

- C_a = calculable part
- $f_{1/A}$ = PDF for parton 1 in hadron of type A

The total (sumation) includes all types of partons. The first term in Equation 3.4 is LO and remainder are higher orders.
PDFs are created by fitting a huge grid of Q^2 and x values from

several tests to a big group of cross section data points. pQCD theory may forecast the mathematical model of PDF but not the actual mathematical form. It can predict Q^2 dependency but not the reliance of PDF on x at a particular Q^2. The major source of PDF determination is data from deep inelastic scattering studies (DIS). When fitting PDFs to data, we choose a starting scale where pQCD assumptions may be applied, and we assume that the PDFs have numerous functional forms. The PDF has been re-parametrized and PDF's $f_j(x_1, \mu_f^2)$ parametrisation came in the form ,

$$f - j(x, \mu_f) = a_0 x^{a^1} (1-x)^{a_2} P(x, a_3, a_4, ..) \tag{3.5}$$

P a polynomial function, and a_j denotes an empirically determined fit value which can't be anticipated theoretically. In the second phase, we select a factorisation scheme that models how heavy quarks are handled, as well as an order of perturbation theory to be employed. Fitting PDFs was done by a number of different groups. The results of MSTW[13] ,CTEQ[21] , NNPDF[38] and ABKM[22] are shown in Figure 3.3. For the fits, they should use all accessible data. The PDF determination method and fitting are dependent on a number of assumptions and uncertainties .

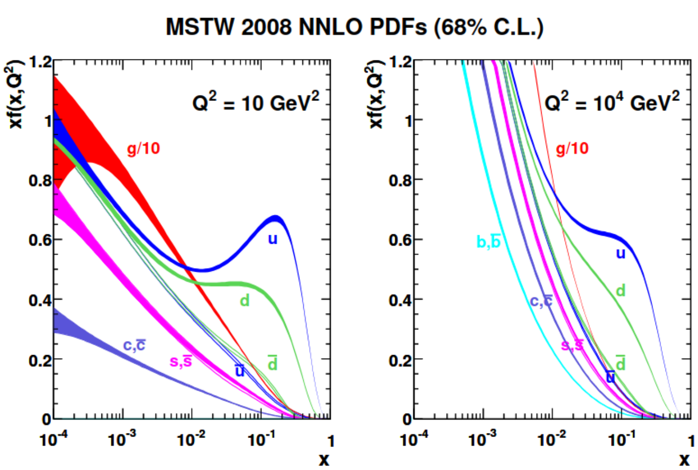

Figure 3.3: PDFs appraise at $m_z^2 = Q^2$,the MSTW 2008 NLO PDF set at $Q^2 = 10^4 GeV^2$ at right and at $Q^2 = 10 GeV^2$ at left [12].

3.4 Flavour schemes

Heavy quark processes, whether in the initial or in the final states, offer an ideal setting for testing our knowledge of pQCD in the presence of many energy scales. There are two main schemes based on either havy quark is in initial, or in final state.

1. Four-Flavour Scheme (4FS)
2. Five-Flavour Scheme (5NFS)

At the matrix element level, a method in which the heavy quark mass is ignored, such a system is known as **five-flavour scheme (5FS)**. In this scheme the contribution of heavy quarks is present in parton PDF.
In **four-flavour scheme (4FS)** system, the heavy quark exists only among the final state particles and is not related to PDF. This scheme is also referred to as massive scheme. In this scheme heavy quarks appear in final state by splittig of gluons (g→ $Q\bar{Q}$).

3.5 MADGRAPH5-MC@NLO

The MADGRAPH5-MC@NLO event generator is a fully automatic MC tool that combines all of MADGRAPH5[24] and AMC@NLO[14] capabilities into a single framework. To achieve parton shower and hadronization effects, it need to be interfaced with a second MC application, such as PYTHIA. MADGRAPH5-MC@NLO has all of the materials required to execute an NLO calculation, perhaps including a parton shower. It provides modules for computing one-loop matrix elements for any kind of processes, as well as a list of potential computations at the LO level. As a result, a few computing options are offered, and they are mentioned explicitly in order of increasing complexity:

- fLO: a calculation at the tree and parton levels, in leading order there is no shower, and the observables are rebuilt using the same particles that occur in the matrix elements.
- fNLO: Except for the perturbative accuracy at NLO, it's the same as fLO. Both tree-level and one-loop matrix elements are used in the computation.

- LO+PS: Parton showers are matched using the matrix elements of the fLO calculation.
- NLO+PS: The only difference between LO+PS and NLO+PS is that the calculation is an NLO instead of a LO. The NLO matrix components are matched with parton showers according to the MC@NLO approach.
- MLM-merged : At the matrix-element level mixes a number of LO+PS samples that differ in terms of final-state multiplicities. The k_T-jet and shower-k_T schemes are two distinct techniques that can be used.
- FxFx-merged : Combine a number of NLO+PS samples with varying final-state multiplicities.

Having each of these diverse simulation options built into MADGRAPH5-MC@NLO, a methodology framework, allows you to study many situations while maintaining consistency. The NLO predictions of MADGRAPH5-MC@NLO were employed in this analysis.

3.5.1 Parton shower and Matrix element

The headon collision of arriving partons, sometimes referred to as "hard scattering" is the initial aspect examined in the modelling of the complete process. Starting with the parton momenta defined by PDFs using Equation 3.1, the hard scattering is characterised using Matrix Element (ME) computations at fixed order in α_s. ME includes high order corrections and final states with many partons in the perturbative computation in power of α_s. Perturbative QCD calculations are no longer practicable due to the divergence of the α_s coupling at low energies. This implies ME can't be used for investigation of a jet's interior composition or structure, and so it is difficult to link it to hadronisation models that take soft partons into account.
To replicate soft and collinear emissions, the Parton Shower (PS) approach is used. Because it uses kinematics, interference, and helicity simplifications, it may generate a random number of gluon or $q\bar{q}$ pair emissions. The first stage is to parameterize a difficult $2 \rightarrow$ n process into a simple $2 \rightarrow 2$ process with showers, where n specifies the number of partons in the final state. PS is based on a

parton splitting and emission sequential stochastic branching model that has been extended till the parton energy scale approaches 1 GeV (usually linked with the production of hadrons). Because the benefits and drawbacks of ME and PS are complimentary, a combination of the two treatments is on the horizon. The key problem in the combined ME+PS simulation is how to deal with phase space overlapping of soft and collinear areas. When more quarks and gluons are incorporated in the ME calculation, this difficulty emerges at the lowest order in α_s. The main concept underpinning the various merging procedures [6] is to reject PS emissions that overlap the ME phase space and apply event weights depending on the probability of ME emissions ordering ("Sudakov form factors") using the splitting functions. ME emissions are preferred over PS emissions because they better characterise hard and angularly separated radiations. At NLO, the PS radiation and the first real emission have a phase space overlap.

3.6 The Z and b production in pp collisions

At the LHC, high-energy protons collide, breaking them apart and allowing scientists to examine their constituents. In comparison to the normal components at lower energies, the up and down quarks, there must be more fascinating stuff in store. Other forms of quark or antiquark (named charm , strange and bottom) occasionally manage to transport a considerable proportion of the proton energy and play a big part in hard scattering due to the intricacy of the binding interactions that hold these together. The generation of a Z boson with a b jet as a result of gluon and/or quark scattering is one such scenario. As a result, such processes offer information about the bottom quark concentration of the proton, as well as aid us in scrutinising theoretical results by comparing expectations to experimental facts. The analysis of these types of collisions is indeed crucial in the context of Higgs boson measurements, as well as in many Beyond Standard Model physics situations. It's no wonder, then, that exact measurements of the rate of creation of $Z+b$ jet(s) events, as well as their attributes, are a crucial aspect of the LHC's physics mission.
The LHC Group has today published the first results on the generation of the $Z+b$ jet(s) in pp collisions at the LHC at a c-o-m energy

of 13 TeV, utilizing data information from the experiments done durring 2016-2018. The decay of the Z boson to oppositely charged μ pairs is used to identify it in the study. The problem is in identifying the b-jets because jets coming from lighter quarks/gluons, which are formed at a much faster pace, can resemble the b-jets. To

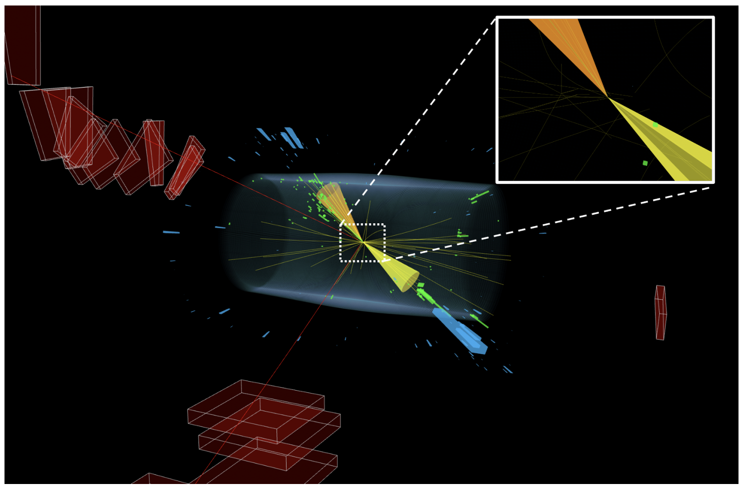

Figure 3.4: An instance of pp interaction. A b-jet (orange cone) and a non-b-jet (yellow cone) accompany the decay of the Z boson to muons (red lines). The figure is taken from [2].

summarize, $Z + b$ jet(s) event rates have been carefully measured as a function of many features, which may be utilized to enhance the theoretical model's prediction. Last but not the least, the considerably uncommon creation of Z + Higgs boson, that can decay to a couple of b quarks. In Higgs production, $Z + b$ jet(s) is might be in background processes. It's been less than a 2-decades since the Higgs boson was found. This reminds us of a well-known quote made more than three decades ago! :

"Yesterday's discovery is today's background".

Maybe in future we find a process in which Higgs production is also in the background processes.

3.7 Measurement of cross section at LHC

The following equation is used to calculate the production cross section in experiments.

$$\sigma = \frac{N_{signal}}{\epsilon BR. \int Ldt} \tag{3.6}$$

where $N_{dat} - N_{bkg} = N_{signal}$ which is equal to signal events observed. The background events are N_{bkg} and selected data events are N_{data}.The efficiency ϵ depends on signal selection criteria ($\epsilon = C.A$, A represents fiducial acceptance factor and C is for detector-induced correction factor) .

3.8 Motivation

This analysis presents studies of bottom quark production related with vector bosons (Z-Boson) at various LHC centre-of-mass energies.

Production of $Z + b$ jet(s)

In investigations of the Standard Model , Higgs boson and searches for non-SM physics, $Z + b$ jet(s) cross-section is an essential benchmark measurement for pQCD phenomenology of heavy quarks and permits limits to be imposed on backgrounds. The parton distribution functions (PDF) in the proton are important in this measurement. Figure 3.5 depicts the leading order diagrams of the $Z + b$ jet(s) process.

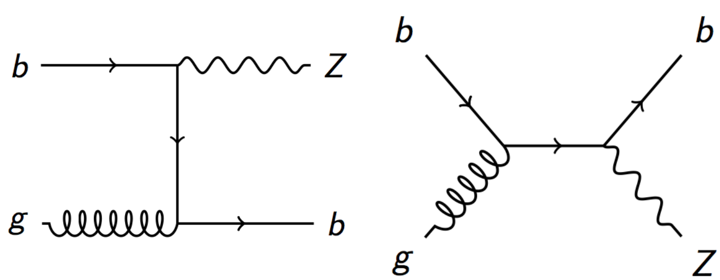

Figure 3.5: Z+b(jet) Feynman diagaram follow 5FNS.

3.9 Event selection for $Z + b$ production

The event for Z+b production is selected in such way that it follow 5FNS and the Z-boson decays to opposite sign and same flavour leptons .i.e. Z $\rightarrow l^+l^-$.

3.9.1 For ATLAS

For ATLAS at 13TeV the Z event is selected in such a way that minimum transverse momentum p_{Tmin} of leptons is greater than 27GeV with pesudo-rapidity not greater than 2.5 having dileptonic mass in the range of 91GeV ± 15GeV.
For selection of b-jet the cutts are : minimum transverse momentum p_{Tmin} is greter than 20GeV with pesudo-rapidity not greater than 2.5 and b-jet and lepton angular distance is greater than 0.4.

Kinematic variables	Acceptance cut
Lepton p_{Tmin}	27GeV< p_{Tmin}
lepton η	2.5> $\|\eta\|$
b-jet p_{Tmin}	20GeV< p_{Tmin}
b-jet rapidity	2.5> $\|y\|$
b-jet-lepton distance	$\Delta R(b - jet, l) > 0.4$
m_{ll}	$m_{ll} = 91GeV \pm 15GeV$

Table 3.1: Cuts on Kinematic for ATLAS analysis, for leptonic channel of Z at 13TeV [1].

3.9.2 For CMS

For CMS at 13TeV the Z event is selected by requiring the minimum leptons transverse momentum p_{Tmin} is greter than 35GeV for leading and 25GeV for sub leading leptons with pesudo-rapidivity not greater than 2.54 having dileptonic mass in the range of 91GeV ± 20GeV.

For selection of b-jet the cuts are : minimum transverse momentum p_{Tmin} is greter than 25GeV with pesudo-rapidity not greater than 2.4, b-jet and lepton angular distance is greater than 0.4 .

Kinematic variables	Acceptance cut
Lepton p_{Tmin} of leading lepton	35GeV< p_{Tmin}
Lepton p_{Tmin} of sub-leading lepton	25GeV< p_{Tmin}
lepton η	2.4> $\|\eta\|$
b-jet p_{Tmin}	25GeV< p_{Tmin}
b-jet rapidity	2.4> $\|y\|$
b-jet-lepton distance	$\Delta R(b-jet, l) > 0.4$
m_{ll}	$m_{ll} = 91GeV \pm 20GeV$

Table 3.2: Cuts on Kinematic for CMS analysis, for leptonic channel of Z at 13TeV [3].

3.10 Measured Cross-Section of Z+b At Different C.O.M Energies

With certain errors ($\pm stat \pm syst \pm theo$), the production cross section of $Z+b$ in pp collisions is measured at LHC in CMS and ATLAS projects at different C.O.M. energies, i.e. 7TeV and 13TeV.
The production cross-section of $Z + b$ predicted, and measured at different C.O.M. energies are listed below in followig Tables 3.3, 3.4, 3.5 and 3.6.

Measured Cross-section ($stat \pm sys \pm theo$)	Predicted Value (value± stat)
3.52 ±0.03 ± 0.22	3.66 ± 0.2

Table 3.3: Predicted and measured values of X-section of $Z + b$ production in CMS analysis, for leptonic channel of Z at 7TeV, using $5fb^{-1}$ of luminosity.

Measured Cross-section ($stat \pm sys \pm theo$)	Predicted Value (value± stat)
4.82 ±0.06 ± 0.02	4.68 ± 0.04

Table 3.4: Predicted and measured values of X-section of $Z + b$ production in ATLAS analysis, for leptonic channel of Z at 7TeV , using $4.6fb^{-1}$ of luminosity.

Measured Cross-section ($stat \pm sys \pm theo$)	Predicted Value (value± stat)
6.52 ±0.04 ± 0.4	7.86 ± 0.51

Table 3.5: Predicted and measured values of X-section of $Z + b$ production in CMS analysis, for leptonic channel of Z at 13TeV, using 19.8fb^{-1} of luminosity.

Measured Cross-section ($stat \pm sys \pm theo$)	Predicted Value (value± stat)
10.9 ±0.031 ± 1.8	11.22 ± 0.19

Table 3.6: Predicted and measured values of X-section of $Z + b$ production in ATLAS analysis.For leptonic channel of Z at 13TeV, using 35.6fb^{-1} of luminosity.

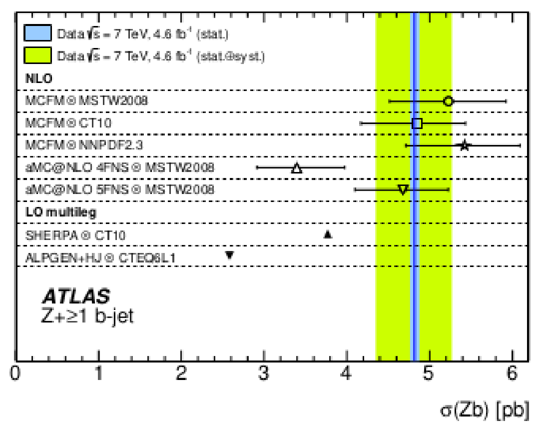

Figure 3.6: Graphical representation of $Z + b$ X-section at 7TeV with 4.6fb^{-1} of integrated lumiosity. The measured value is shown by blue line while blue band is showing the statistical uncertainity.The green band showing total sum of systematic and statistical uncertainties. And also MCFM and aMC@NLO (using same set of PDFs) predictions are shown.[25]

3.11 Uncertainties in Predictions

The major source of uncertainty in forecasts is, incomplete understanding of the proton parton PDFs. The PDF's uncertainties may be calculated by subtracting the difference between the central PDF

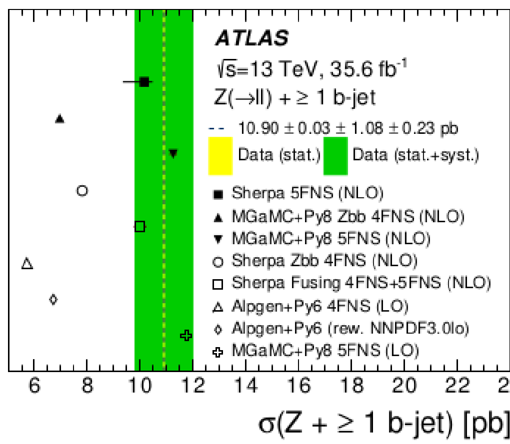

Figure 3.7: Graphical representation of $Z + b$ X-section at 13TeV. The measured value is shown by central dotted line while the yellow band is showing the statistical uncertainity. The green band showing total sum of systematic and statistical uncertainties. And predicted X-section of different generators at 13TeV for luminosity of $35.6fb^{-1}$ are shown [1].

and the error vectors of the corresponding PDF set from the sum in quadrature . The uncertainty calculation is dependent on the provided PDF set; for example, the MC replicas set (NNPDF) has a different way of uncertainty determination than the PDF set having Hessian uncertainites , and the same is true for all other PDF sets. comutation mathod of monte carlo and hessian uncertainites are explain in next two sub-sections.

3.11.1 Monte Carlo uncertainties Calculation

A PDFs collection with replicas is provided for the Monte Carlo PDF set i.e. NNPDF. For any observable A (in our case cross-section) the average value that is dependent on PDF sets is calculated using standard relation given by,

$$< A >= \frac{\sum_{i=1}^{N_{mem}} A^{(i)}}{N_{mem}} \tag{3.7}$$

Total members in MC replicas are represented by N_{mem}. According to the standard relation , the related uncertainty in the observable is determined [7] by,

$$\delta^{pdf} A = \sqrt{\frac{\sum_{i=1}^{N_{mem}} (A^{(i)} - < A >)^2}{N_{mem} - 1}} \tag{3.8}$$

Equation 3.8 is just a simple calculation of standard deviation which gives us uncertainity in MC replicas of given PDF set having N_{mem} of total members.

3.11.2 Hessain uncertainties Calculation

Both central and error sets are provided for Hessian PDF sets. The number of free parameters is equal to the number of eigenvectors. The experimental uncertainties are transmitted using the hessian matrix technique by diagonalizing the $n \times n$ Hessian matrix ; further information may be found in [7]. Consider a variable A, A_0 is it's central value which can be determined by using given PDF set . A^+ is it's value in positive and A^- is it's value in negative direction of error vector i [7].

$$\Delta A^+ = \sqrt{\sum_{i=1}^{N} [max(A_i^+ - A_0, A_i^- - A_0, 0)]^2} \tag{3.9}$$

$$\Delta A^- = \sqrt{\sum_{i=1}^{N} [max(A_0 - A_i^+, A_0 - A_i^-, 0)]^2} \tag{3.10}$$

The PDF error ΔA^+ shows that the observable Y has increased, whereas the PDF error ΔA^- indicates that the observable Y has decreased. The total sum is over all the numbers of eigenvector directions (N).

Hessian Symmetry: The central value and PDF uncertainties are determined as by Equation 3.11 for the basic symmetric situation when just the value of variable using central PDF A_0 and N error vectors using PDF A_i (i= 1,..., N) are given,

$$\Delta A^+ = \Delta A^- = \Delta A = \sqrt{\sum_{i=1}^{N} (A_i - A_0)^2} \tag{3.11}$$

3.11.3 Theoretical Uncertainties

The relationship between the PDF and measurable quantities is improved when theoretical uncertainties are determined. Experimental uncertainty research is far more advanced than theoretical uncertainty research, with just a few theoretical uncertainties examined in depth. The first source of theoretical uncertainty is the determination of strong interaction between quarks. The value of the strong coupling constant α_s, the heavy quark weights m_c (charmquarks) and m_b (bottomquarks), and the variation of the renormalisation μ_r and factorisation scales μ_f are all sources of theoretical errors in QCD. Each PDF group investigates the uncertainty caused by the choice of the coupling constant α_s value in depth. Some PDF groups, such as NNPDF3.1, Cteq18, HERA, and others, have looked at the uncertainty caused by the choice of heavy quark weights (charm and bottom). NNPDF3.1 investigates the uncertainties caused by differences in factorisation and re-normalisation scales.

3.11.3.1 The α_s and it's uncertainity

Each PDFs group investigates the theoretical uncertainty caused by choice of α_s value. As seen in Figure 3.8, various PDF groups employed different values of α_s . For the calculation of α_s uncertanities

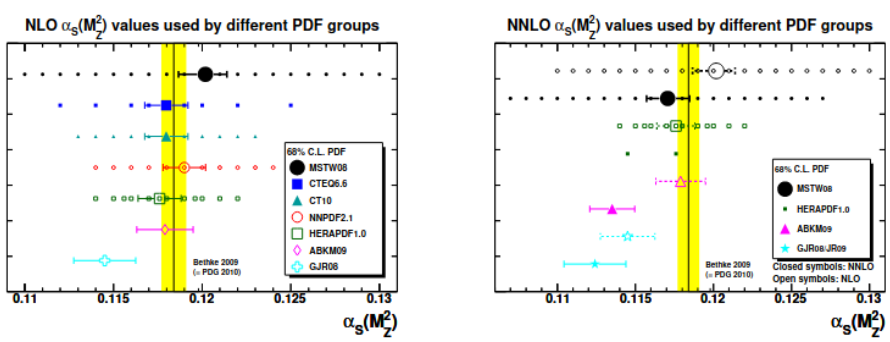

Figure 3.8: Various PDF groups use different values for α_s. The figure is taken from referance [7].

we use any PDFs with some central referance value of α_s and calculate cross-section at that value.
Current PDG average of α_s is 0.1187 $\pm$0.0007. Then we need to cal-

culate cross-sections for all the error sets of that PDF set at given appropiate different values of α_s. Find the difference from central value and add all differences in quadrature.

$$\delta^{\alpha_s}\sigma = \sqrt{\sum_{i}^{\alpha_{smax}} (\sigma_{\alpha_0} - \sigma_{\alpha_i})^2} \tag{3.12}$$

3.11.3.2 PDF+α_s uncertainities

For the calculation of α_s + PDF uncertanities, one should first calculate PDF uncertainity at the central value of α_s (fixed). And calcuate α_s uncertainity at fixed PDF and add them in quadrature for combined uncertainity.

$$\delta\sigma^{pdf+\alpha_s} = \sqrt{(\delta\sigma^{pdf})^2 + (\delta\sigma^{\alpha_s})^2} \tag{3.13}$$

where $\delta\sigma^{pdf}$ is PDF uncertainty and $\delta\sigma^{as}$ is α_s uncertainty in cross-section . $\delta\sigma^{pdf+\alpha_s}$ is the combined PDF+α_s uncertainty.

Chapter 4

Results and Discussion

In this thesis, using different PDF sets (CT10, CT14 , NNPDF3.1 , HERAPDF and ABMP) we made a comparison between experimentally observed production cross section (σ) of $Z+b$ ($Z \to \mu^+\mu^-$) and theoretical predicted cross section of $Z+b$ ($Z \to \mu^+\mu^-$). The cross-section is predicted at both Leading-Order (LO) and Next-to-Leading Order (NLO). The uncertainties in cross-section due to PDFs and α_s are measured. The combined PDFs and α_s uncertainties are also measured. The change in Cross-Section due to variation in QCD dynamical scales (eenormalization μ_R and factorization μ_F) is also measured. The uncertainties in prediction are measured at 13TeV , 13.6TeV and 14TeV . The kinematics of $Z+b$ processes , Transverse momentum (p_T) and Pseudo rapidity (η) for both Z and b-jet are predicted. For the prediction we used MADGRAPH5-MC@NLO event generator interfaced with LHAPDF and Pythia8.

4.1 PDF NNPDF3.1

A precise knowledge of PDF was crucial in the search of Higgs boson at LHC, and it also provides valuable insight into the search for novel physics at LHC. The most newest PDF collection is NNPDF3.1, which is an upgrade from NNPDF3.0 and is available in LO, NLO, and NNLO accuracy. In Figure 4.1 LO plots, Figure 4.2 shows NLO and Figure 4.3 shows NNLO plots for NNPDF3.1 at different values of $\mu_F = Q^2$.

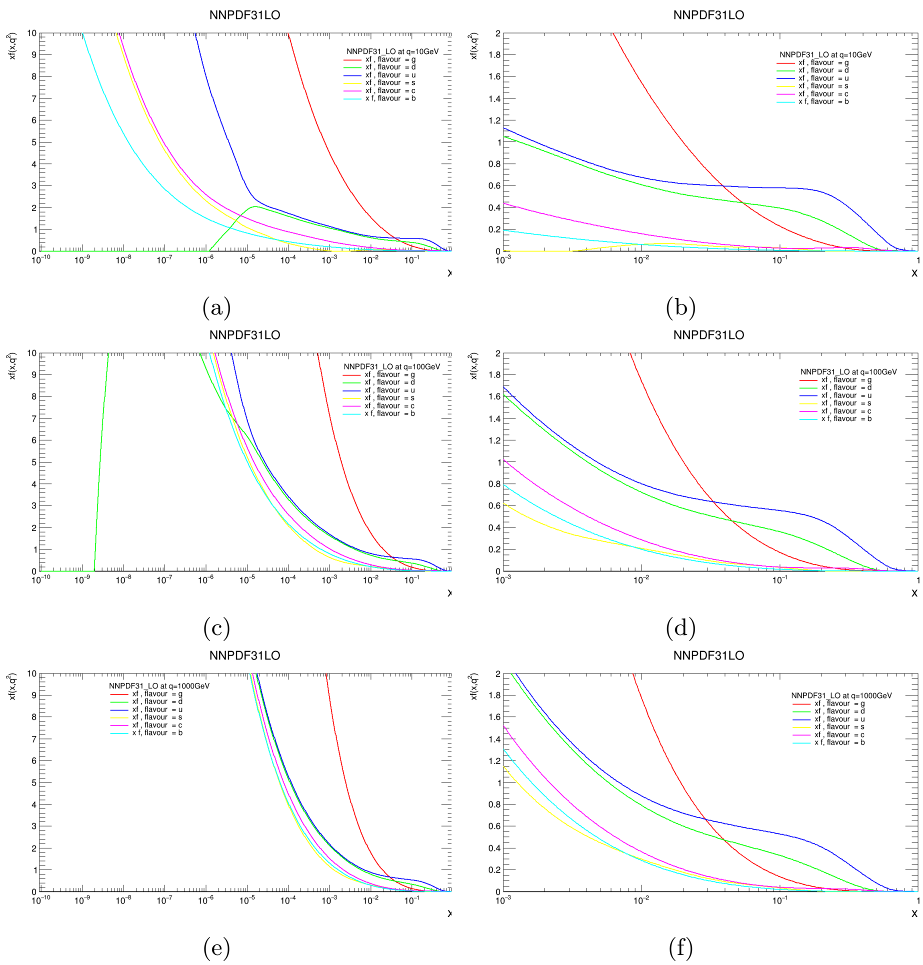

Figure 4.1: NNPDF3.1-LO PDF plots for quarks (b (bottom), c (charm), s (strange), u (up), d (down)) and g (gluon). (a),(b) For $Q^2 = 10GeV$, (c),(d) For $Q^2 = 100GeV$ and (e),(f) For $Q^2 = 1000GeV$.

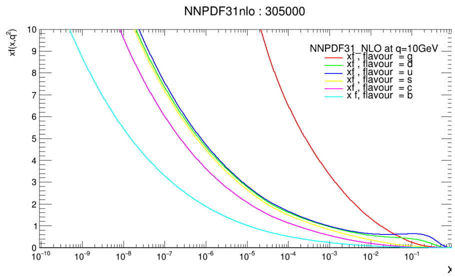

(a)

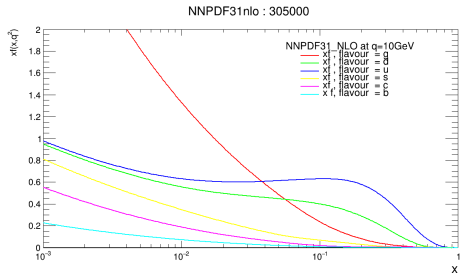

(b)

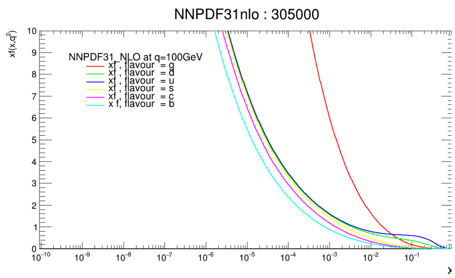

(c)

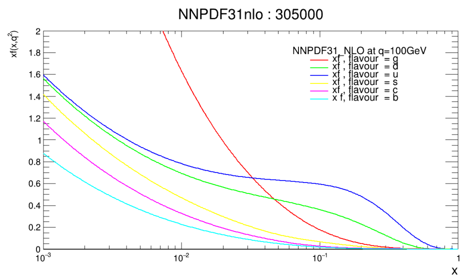

(d)

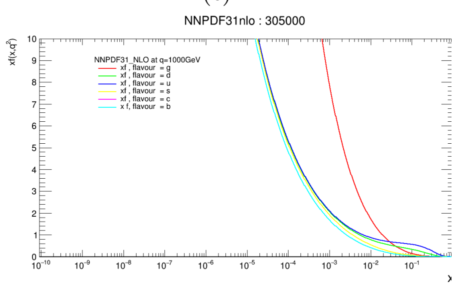

(e)

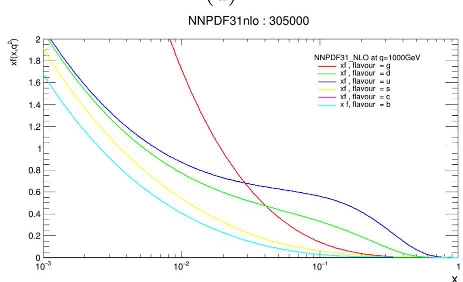

(f)

Figure 4.2: NNPDF3.1-NLO PDF plots for quarks (b (bottom), c (charm), s (strange), u (up), d (down)) and g (gluon). (a),(b) For $Q^2 = 10GeV$, (c),(d) For $Q^2 = 100GeV$ and (e),(f) For $Q^2 = 1000GeV$.

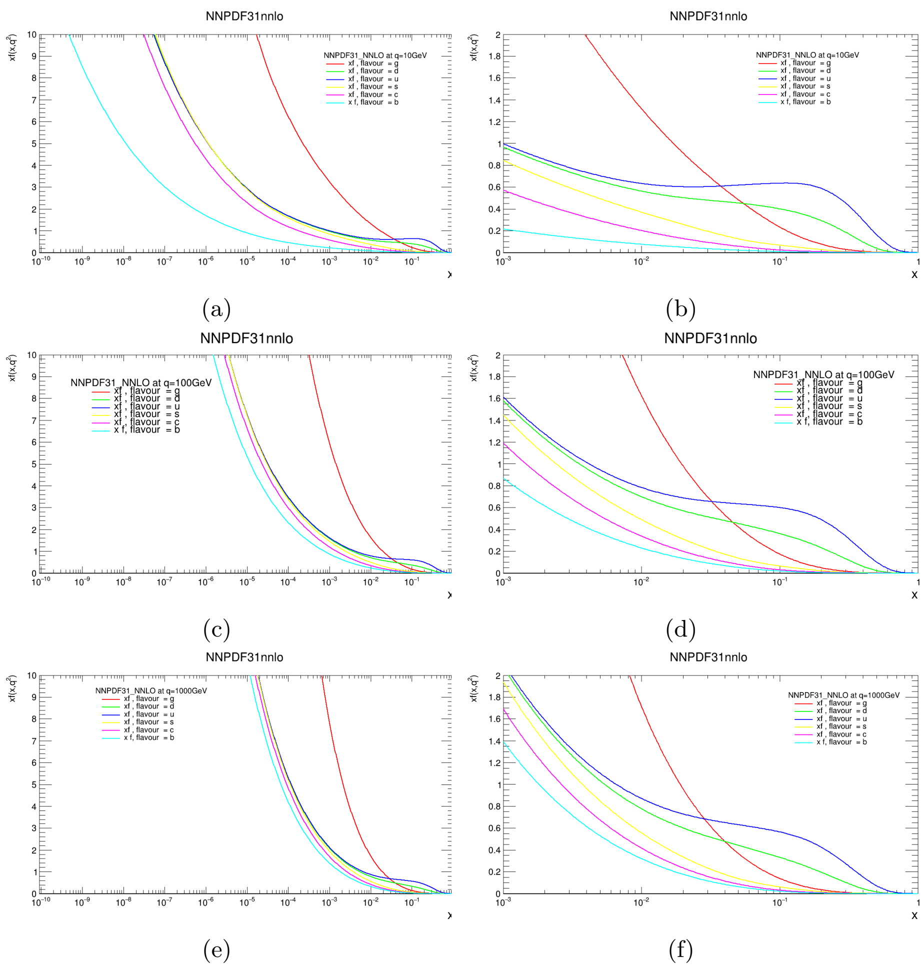

Figure 4.3: NNPDF3.1-NNLO PDF plots for quarks (b (bottom), c (charm), s (strange), u (up), d (down)) and g (gluon). (a),(b) For $Q^2 = 10GeV$, (c),(d) For $Q^2 = 100GeV$ and (e),(f) For $Q^2 = 1000GeV$.

4.2 Predictions and Measurments

The theoretical predictions are compared to the measurements of the production cross-section ($\sigma_{(Z+b)}$) of $Z + b$. At 13TeV in proton-proton collisions, the cross sections are determined using both CMS and ATLAS data.
The production cross-section of $Z + b$ $\sigma_{(Z+b)}$) is also theoretically predicted for 13TeV, 13.6TeV and 14TeV center of mass energies and

we also made a comparison with previous results obtained at 7 TeV. We use NNPDF3.1, CT10, CT14 and HERAPDF20 for theoretical predictions. We also calculate uncertainties in prdicted values.

4.2.0.1 Results

4.2.0.1.1 Comparison at 7TeV

The production cross-section of $Z+b$, predicted and measured, at 7TeV of C.O.M. energy is listed below in Table 4.1 . The uncertainty in measured values are due to statistical, systematic and luminosity errors.

Measured Cross-section [pb] ($stat \pm sys \pm theo$)	Predicted Value [pb] (value± stat)
4.82 ±0.06 ± 0.02	4.68 ± 0.04

Table 4.1: Predicted and measured values of X-section of $Z+b$ production for ATLAS analysis. For leptonic channel of Z at 7TeV , with 4.6fb^{-1} of luminosity [25].

4.2.0.1.2 Comparision at 13TeV

The production cross-section of $Z+b$, predicted and measured ,at 13TeV of C.O.M. energy by using different PDF sets is listed below in Table 4.2 . The uncertainty in the measured values are due to statistical, systematic and luminosity errors. For predictions NNPDF3.1NLO , CT10NLO , CT14NLO , and HERAPDF20 are used.

Measured Cross-section [pb] ($stat \pm sys \pm theo$)	PDF set	Predicted Value [pb] (value± stat)
10.9 ±0.031 ± 1.8	NNPDF3.1NLO	11.22 ± 0.19
	CT10NLO	10.07 ± 0.15
	CT14NLO	11.22 ± 0.18
	HERAPDF20	10.95 ± 0.17

Table 4.2: Predicted and measured values of X-section of $Z+b$ production for ATLAS analysis. For leptonic channel of Z at 13TeV, with 35.6fb^{-1} of luminosity [1].

Figure 4.4 shows the measured value of cross section at 13TeV and predicted values for different PDFs along with uncertainties graphecally .

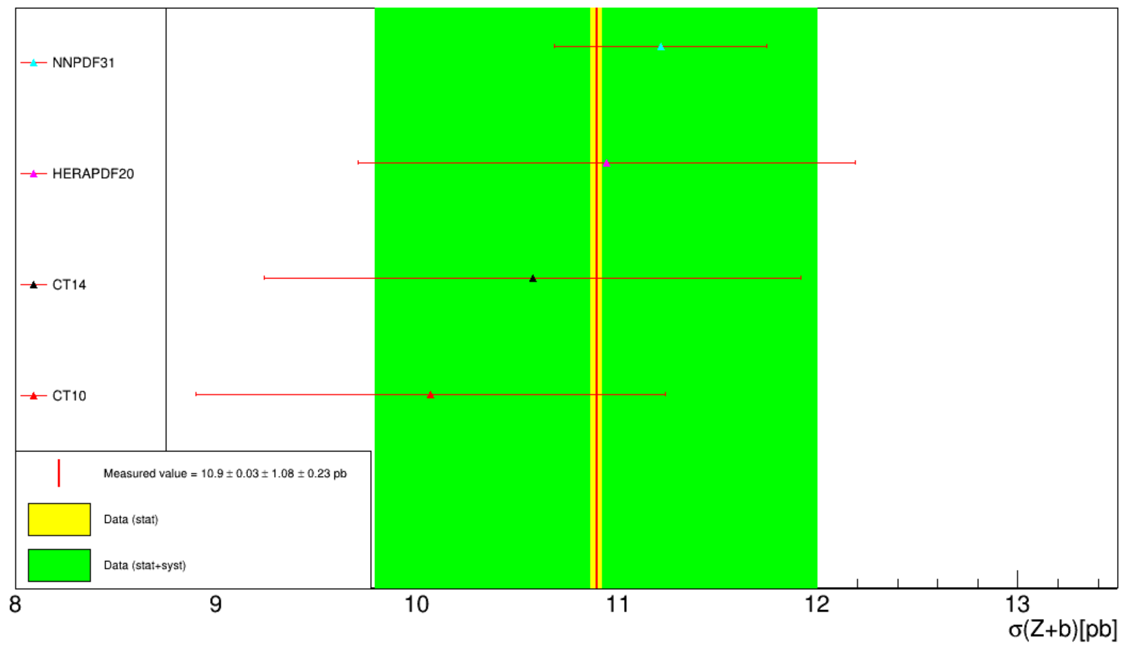

Figure 4.4: The graphical representation of measured value of $Z+b$ cross section ($\sigma_{(Z+b)} = 10.9 \pm 0.031 \pm 1.8$ with luminosity of $35.6fb^{-1}$ [1] and predicted values of cross section by using NNPDF3.1NLO , CT10NLO , Ct14NLO , and HERAPDF20 PDF sets. The verticle red line shows mean measured value , while inner yellow band shows statistical uncertainty and outer green bar shows total uncertainity in measured value. Different points on graph represent different PDFs values and red horizontal lines show total uncertainity in predicted values as a sum in quadrature.

4.3 Predictions and uncertainties in cross-section of $Z + b$ production at 13TeV.

The predicted cross section of $Z + b$ in pb is presented with varying levels of uncertainty. Both Monte-Carlo replicas and the Hessian error eigen vector approach are used to calculate the errors. The

correlation between the variance in QCD scale and the variation in predictions is also determined.
The results of predicted cross-section and uncertainites at 13TeV for different sets of PDF are shown in Figure 4.5 .
The variation of cross-section by changing the value of $\alpha_s(M_Z^2)$ is shown in Figure 4.6.
Change in predicted cross-section by changing QCD scales (μ_F and μ_R) are shown in Figure 4.7 for CT10 and NNPDF31

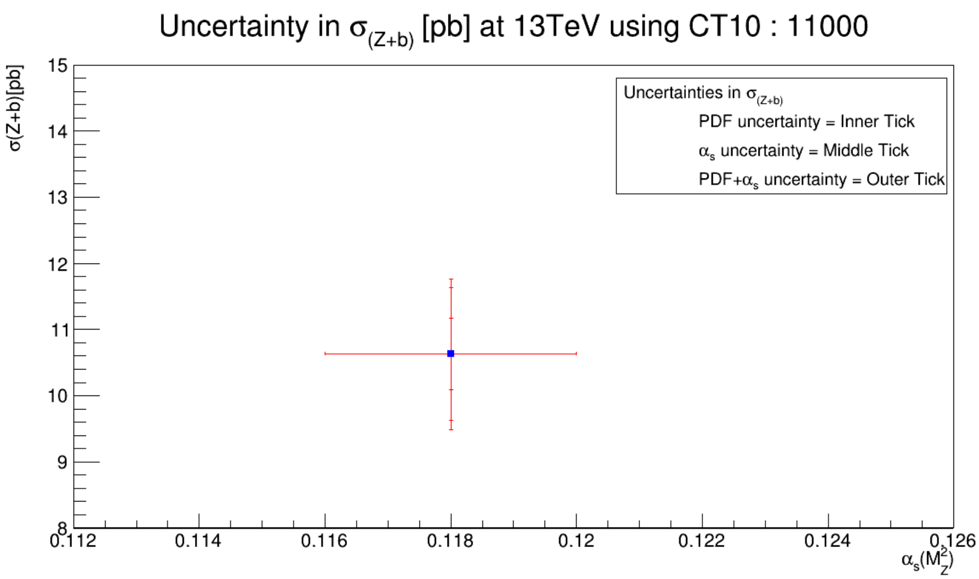
Uncertainty in $\sigma_{(Z+b)}$ [pb] at 13TeV using CT10 : 11000
σ(Z+b)[pb]
Uncertainties in $\sigma_{(Z+b)}$
PDF uncertainty = Inner Tick
α_s uncertainty = Middle Tick
PDF+α_s uncertainty = Outer Tick
$\alpha_s(M_Z^2)$

(a)

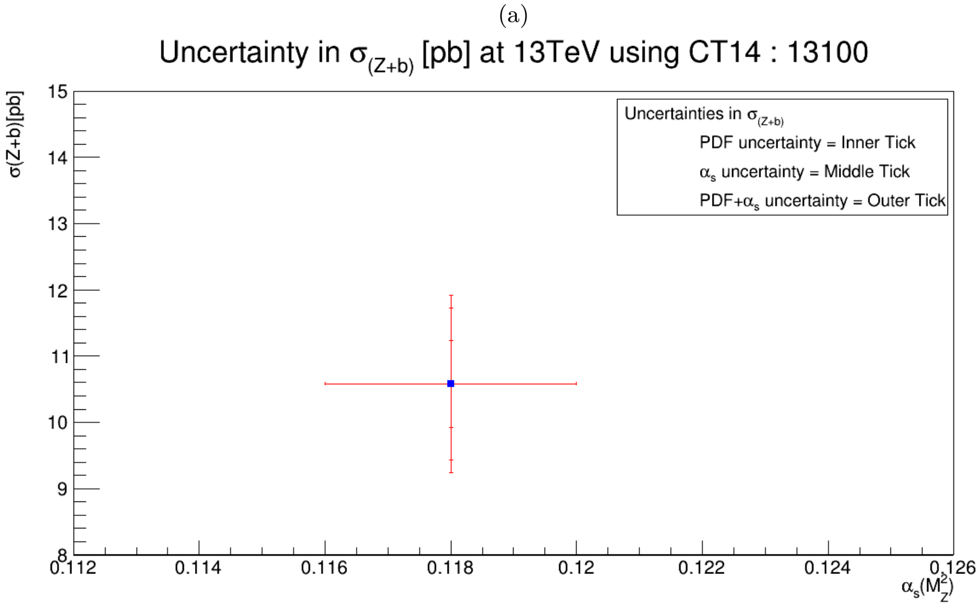
Uncertainty in $\sigma_{(Z+b)}$ [pb] at 13TeV using CT14 : 13100
σ(Z+b)[pb]
Uncertainties in $\sigma_{(Z+b)}$
PDF uncertainty = Inner Tick
α_s uncertainty = Middle Tick
PDF+α_s uncertainty = Outer Tick
$\alpha_s(M_Z^2)$

(b)

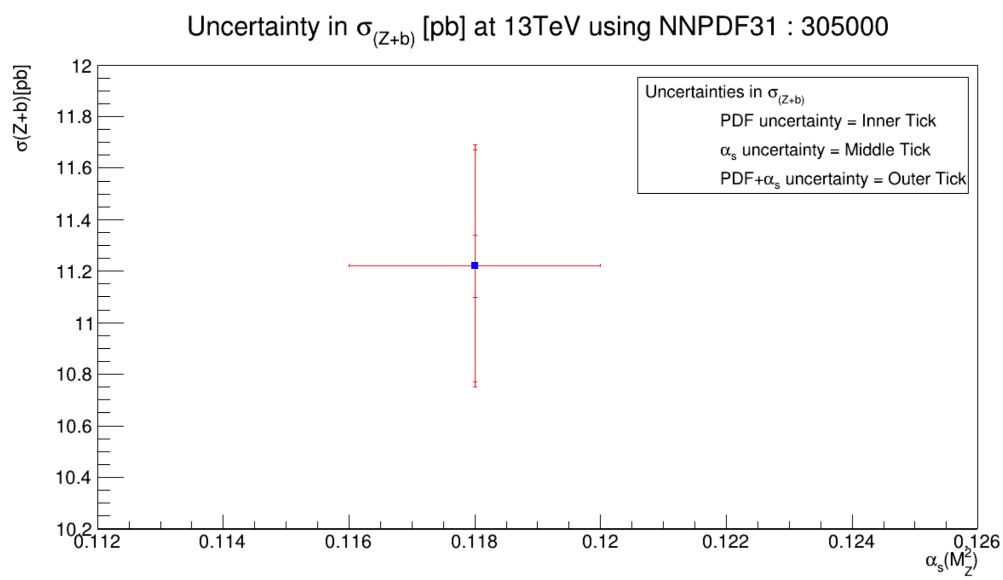

(c)

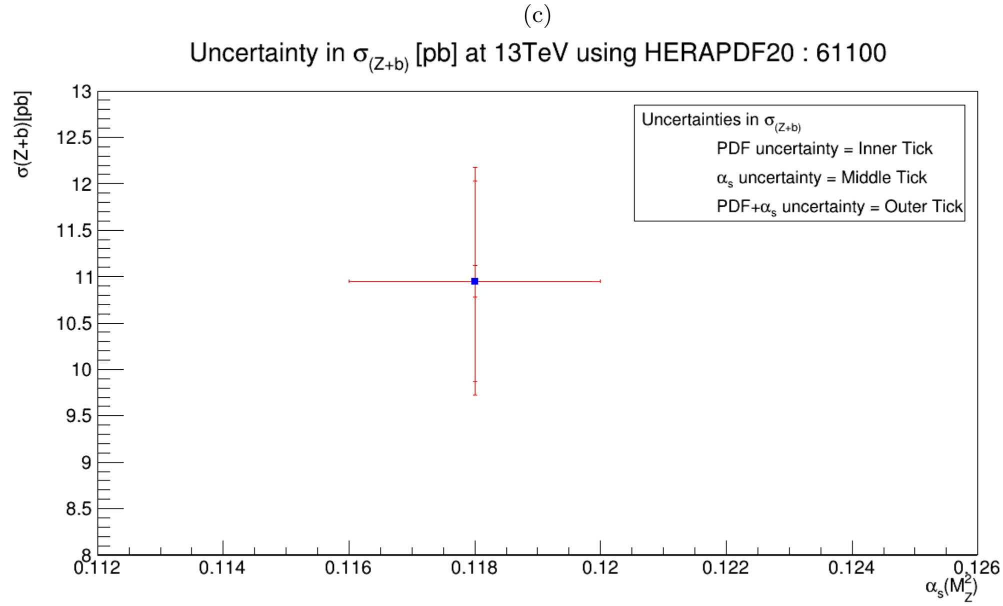

(d)

Figure 4.5: The plot (a) shows predicted cross-section and uncertainities ($pdf \pm \alpha_s \pm pdf + \alpha_s$) in cross-section by using CT10 , The plot (b) shows predicted cross-section and uncertainities ($pdf \pm \alpha_s \pm pdf + \alpha_s$) in cross-section by using CT14 , The plot (c) shows predicted cross-section and uncertainities ($pdf \pm \alpha_s \pm pdf + \alpha_s$) in cross-section by using NNPDF31 and The Figure 4.5d shows predicted cross-section and uncertainities ($pdf \pm \alpha_s \pm pdf + \alpha_s$) in cross-section by using HERAPDF20 .

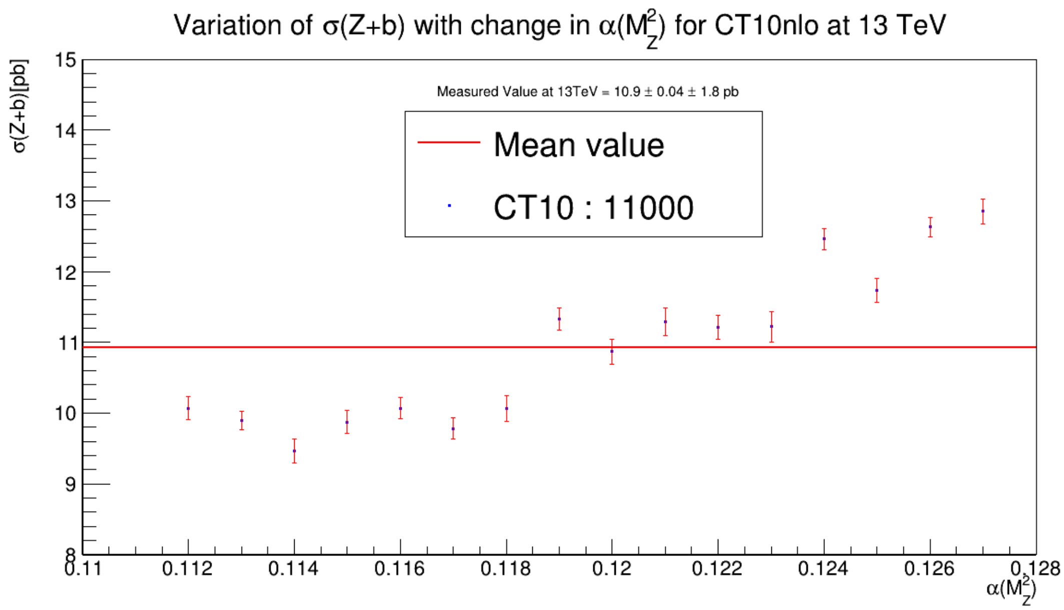
Variation of σ(Z+b) with change in α(M$_Z^2$) for CT10nlo at 13 TeV
Measured Value at 13TeV = 10.9 ± 0.04 ± 1.8 pb
Mean value
CT10 : 11000
σ(Z+b)[pb]
α(M$_Z^2$)

(a)

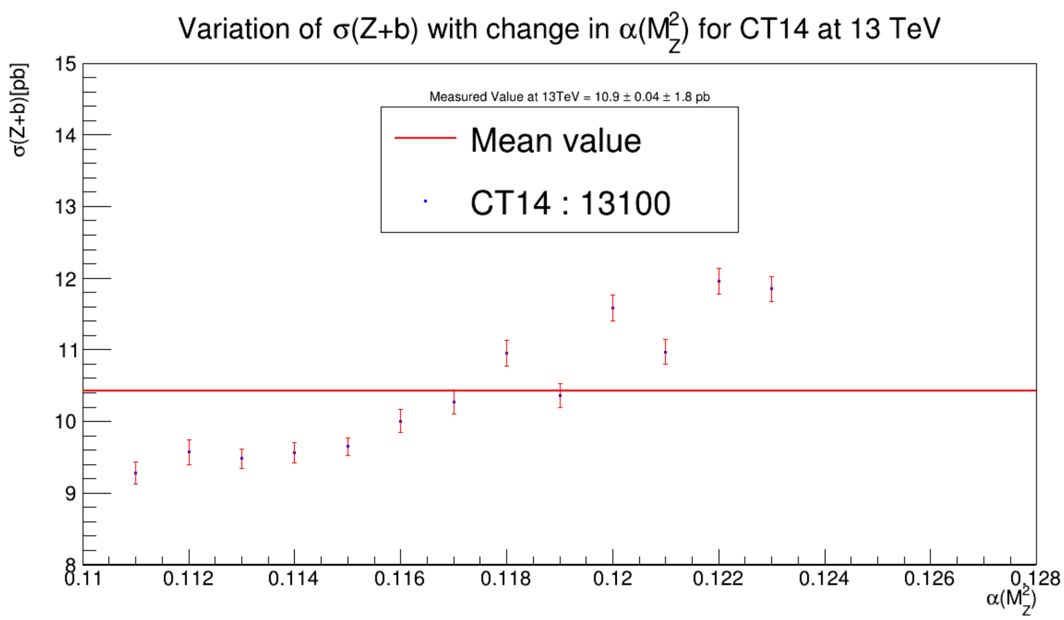
Variation of σ(Z+b) with change in α(M$_Z^2$) for CT14 at 13 TeV
Measured Value at 13TeV = 10.9 ± 0.04 ± 1.8 pb
Mean value
CT14 : 13100
σ(Z+b)[pb]
α(M$_Z^2$)

(b)

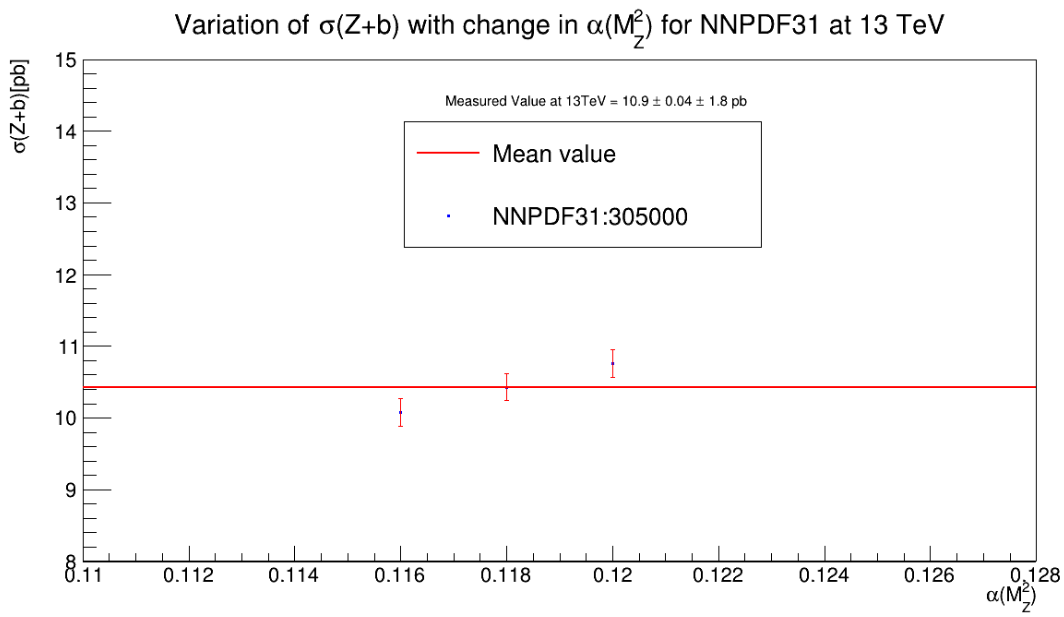

(c)

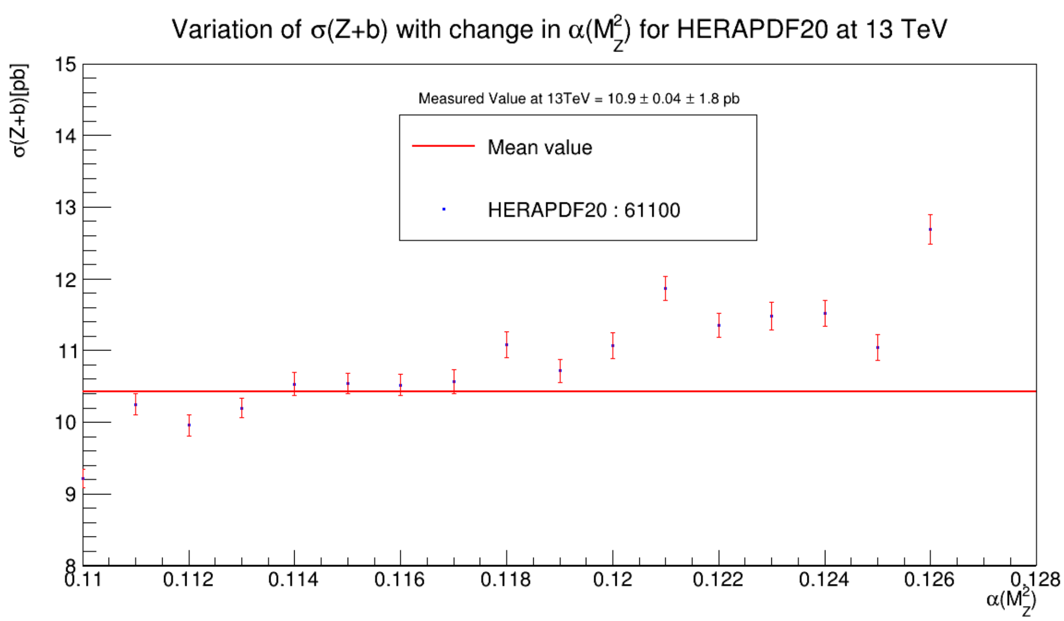

(d)

Figure 4.6: Plot (a) shows variation in cross-section for CT10nlo, plot (b) shows variation in cross-section for CT14nlo , plot (c) shows variation in cross-section for NNPDF31nlo and plot (c) shows variation in cross-section for HERAPDF20 , with respect to change in choice of $\alpha_s(M_Z^2)$. The verticle bars represents PDF uncertainity and red line represent average value of cross-section for respective PDFs.

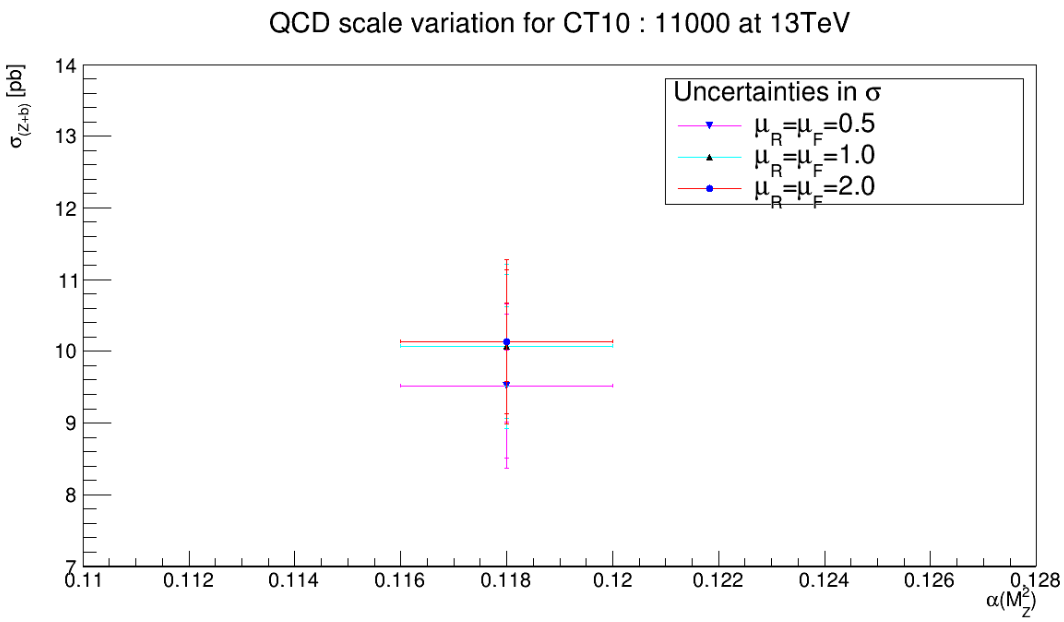

QCD scale variation for CT10 : 11000 at 13TeV
σ(Z+b) [pb]
Uncertainties in σ
μR=μF=0.5
μR=μF=1.0
μR=μF=2.0
α(M²Z)

(a)

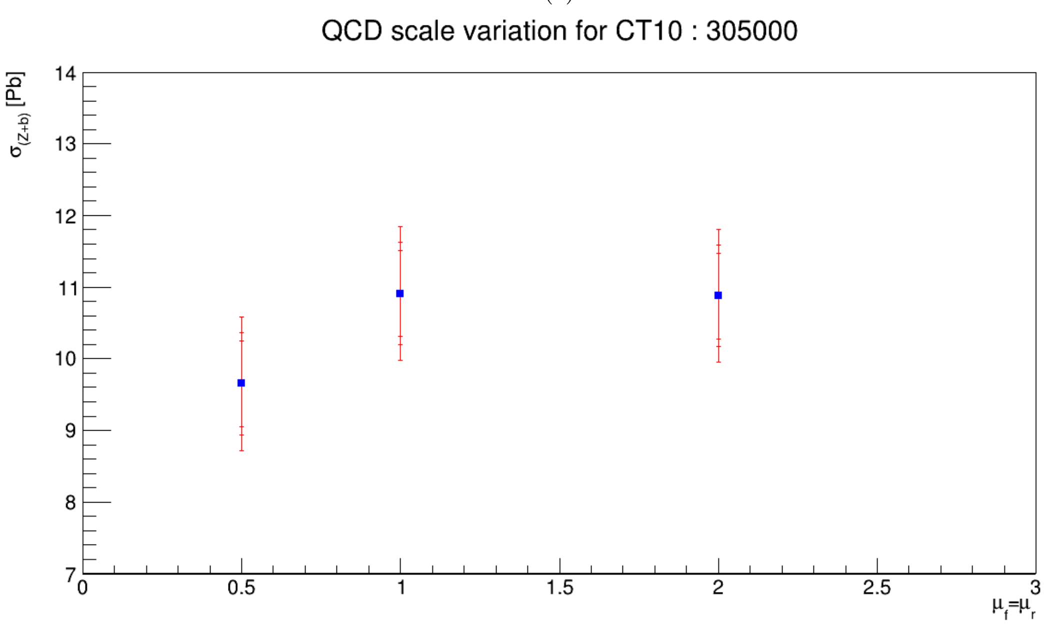

QCD scale variation for CT10 : 305000
σ(Z+b) [Pb]
μf=μr

(b)

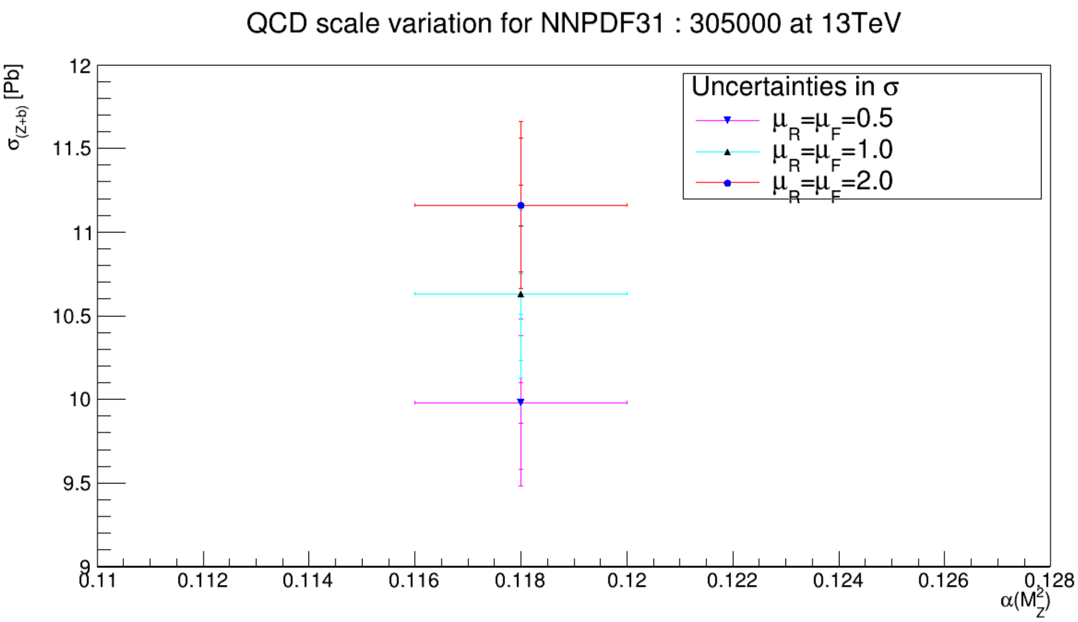

(c)

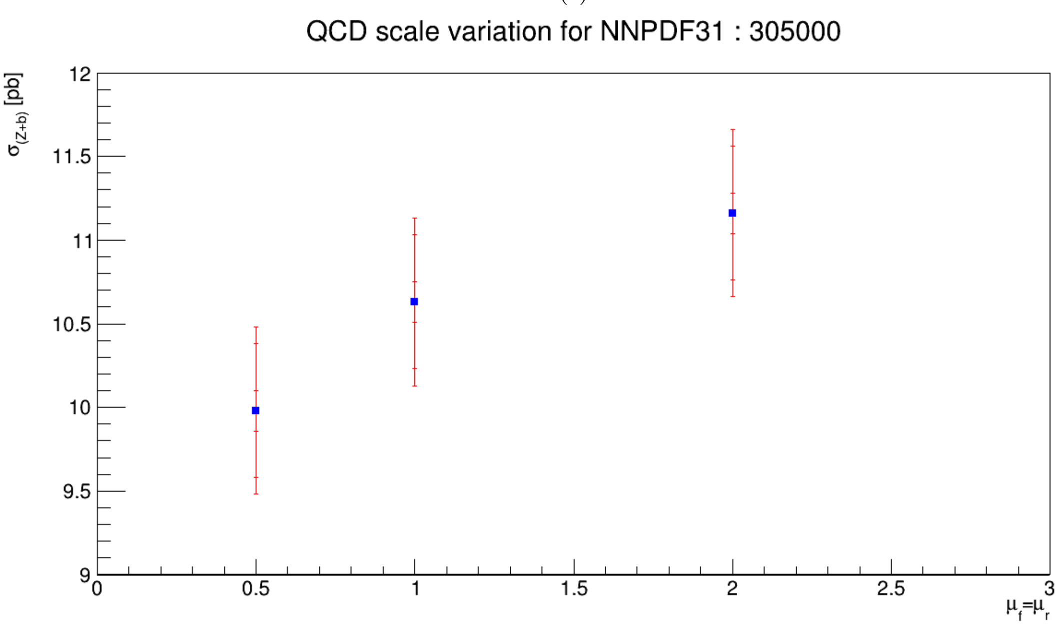

(d)

Figure 4.7: (a) and (b) shows value of cross-section at different values of QCD scales for CT10 PDF while (c) and (d) show value of cross-section at different values of QCD scales for NNPDF31 PDF. Inner bars represent pdf, middle bar represent α_s and outer bar represent pdf+α_s uncertainties.

4.4 Predictions and uncertainties in cross-section of Z+b production at 13.6TeV.

The production cross-section of $Z + b$ predicted at 13.6TeV C.O.M. energy by using different PDF sets is listed below in Table 4.3 . For predictions NNPDF3.1NLO , CT10NLO , Ct14NLO , and HERA-PDF20 are used.

Measured Cross-section [Pb]	PDF set	Predicted Value [Pb] (value± stat)
Not yet measured	NNPDF3.1NLO	11.51 ± 0.24
	CT10NLO	10.91 ± 0.18
	CT14NLO	10.97 ± 0.18
	HERAPDF20	11.77 ± 0.19

Table 4.3: Predicted values of X-section of Z+b production For leptonic channel of Z at 13.6TeV .

The results of predicted cross-section and uncertainties at 13.6TeV for different sets of PDF are shown in Figure 4.8 .

The variation of cross-section by changing the value of $\alpha_s(M_Z^2)$ is shown in Figure 4.9 .

Change in predicted cross-section by changing QCD scales (μ_F and μ_R) is shown in Figure 4.10 for CT10 and NNPDF31.

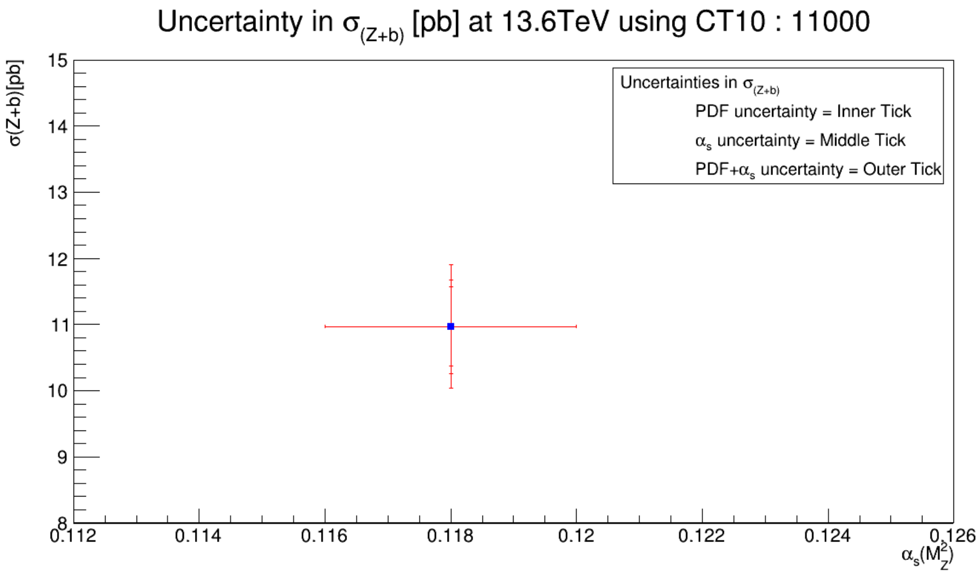
Uncertainty in σ(Z+b) [pb] at 13.6TeV using CT10 : 11000
σ(Z+b)[pb]
Uncertainties in σ(Z+b)
PDF uncertainty = Inner Tick
αs uncertainty = Middle Tick
PDF+αs uncertainty = Outer Tick
15
14
13
12
11
10
9
8
0.112
0.114
0.116
0.118
0.12
0.122
0.124
0.126
αs(M²Z)

(a)

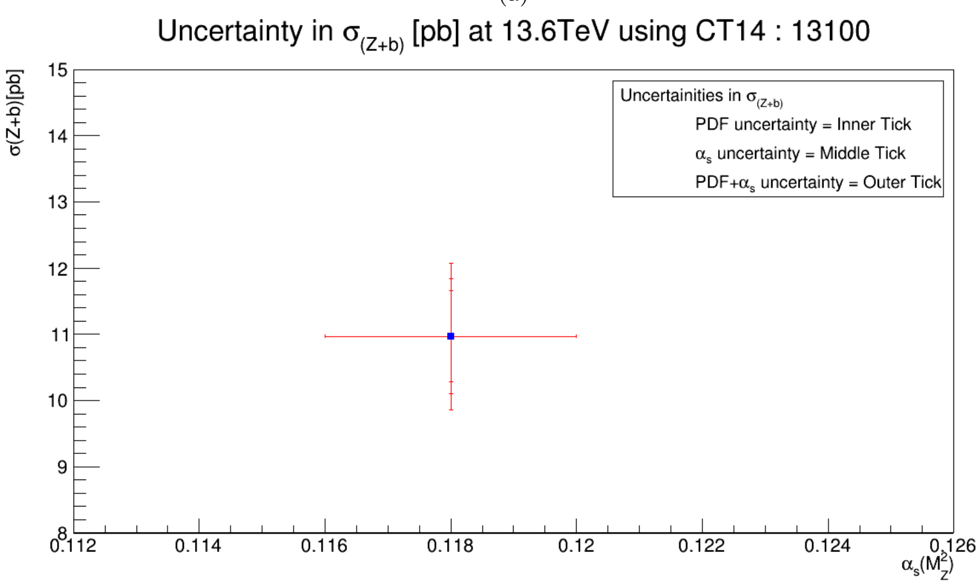
Uncertainty in σ(Z+b) [pb] at 13.6TeV using CT14 : 13100
σ(Z+b)[pb]
Uncertainities in σ(Z+b)
PDF uncertainty = Inner Tick
αs uncertainty = Middle Tick
PDF+αs uncertainty = Outer Tick
15
14
13
12
11
10
9
8
0.112
0.114
0.116
0.118
0.12
0.122
0.124
0.126
αs(M²Z)

(b)

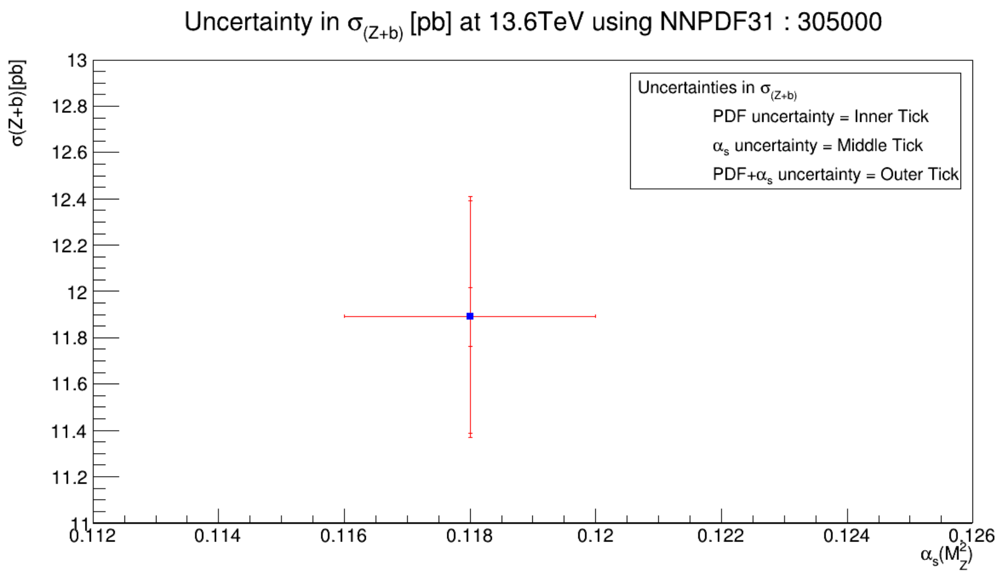

(c)

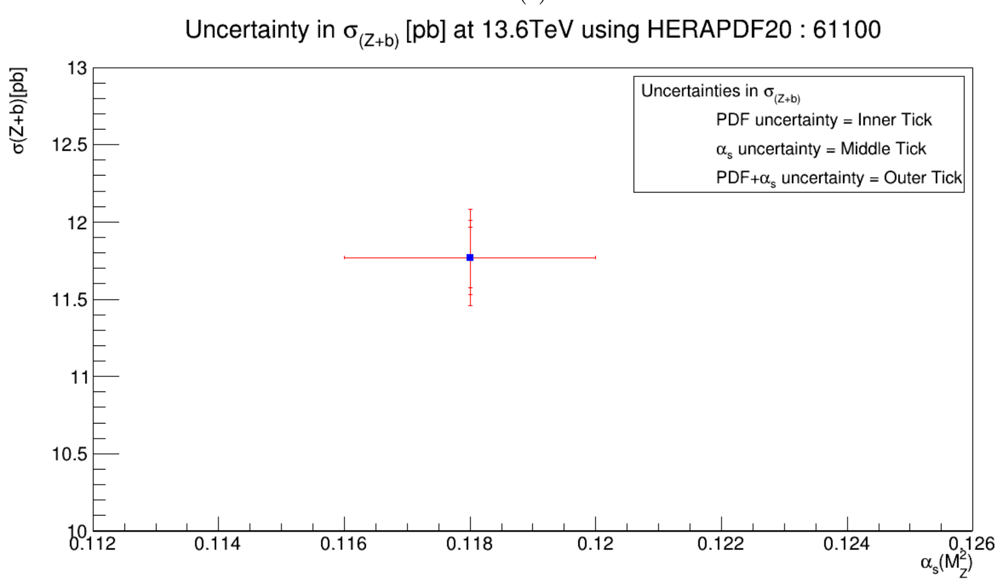

(d)

Figure 4.8: Plot (a) shows predicted cross-section and uncertainities ($pdf \pm \alpha_s \pm pdf + \alpha_s$) in cross-section by using CT10 , plot (b) shows predicted cross-section and uncertainties ($pdf \pm \alpha_s \pm pdf + \alpha_s$) in cross-section by using CT14 , plot (c) shows predicted cross-section and uncertainties ($pdf \pm \alpha_s \pm pdf + \alpha_s$) in cross-section by using NNPDF31 and plot (d) shows predicted cross-section and uncertainties ($pdf \pm \alpha_s \pm pdf + \alpha_s$) in cross-section by using HERAPDF20 .

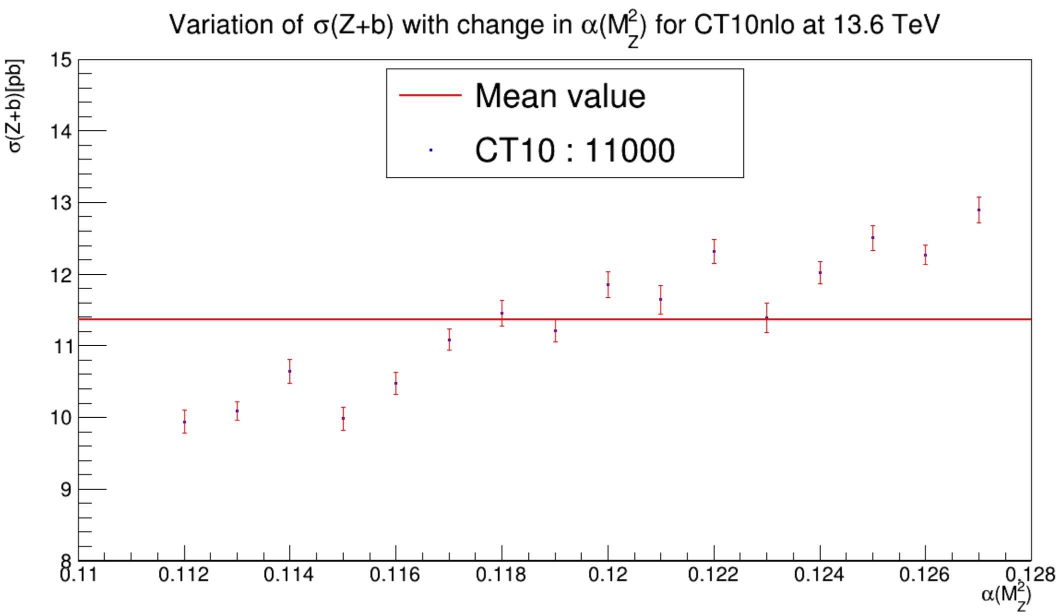

Variation of σ(Z+b) with change in α(M_Z^2) for CT10nlo at 13.6 TeV
σ(Z+b)[pb]
Mean value
CT10 : 11000
15
14
13
12
11
10
9
8
0.11
0.112
0.114
0.116
0.118
0.12
0.122
0.124
0.126
0.128
α(M_Z^2)

(a)

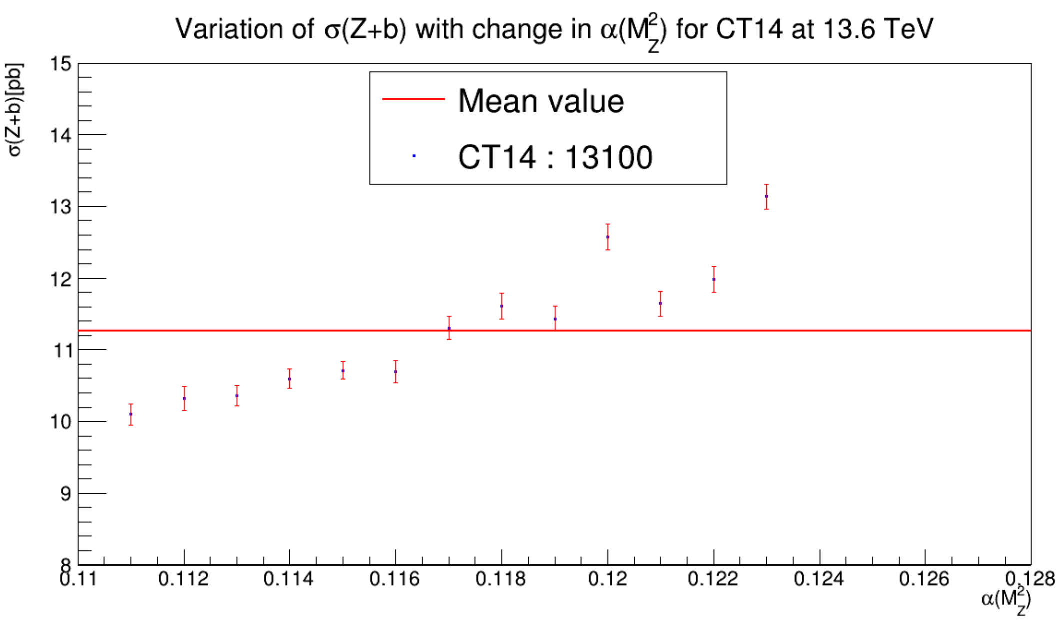

Variation of σ(Z+b) with change in α(M_Z^2) for CT14 at 13.6 TeV
σ(Z+b)[pb]
Mean value
CT14 : 13100
15
14
13
12
11
10
9
8
0.11
0.112
0.114
0.116
0.118
0.12
0.122
0.124
0.126
0.128
α(M_Z^2)

(b)

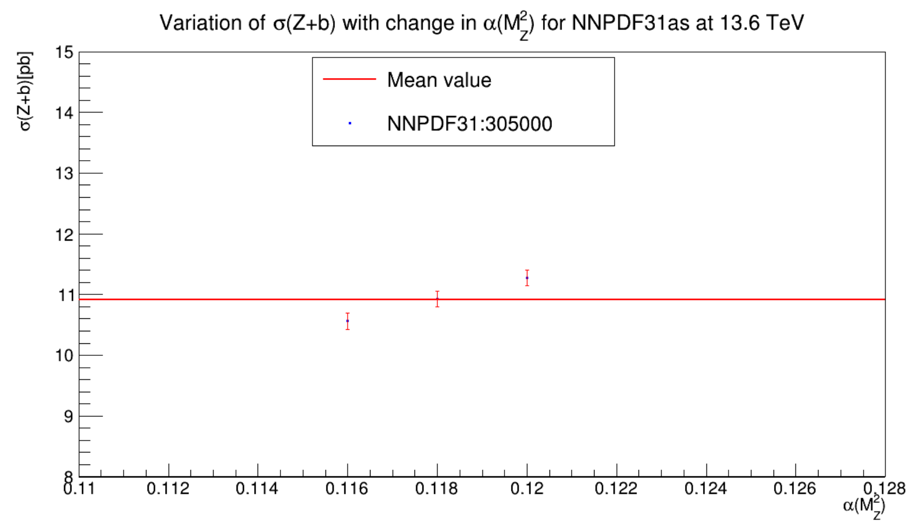

(c)

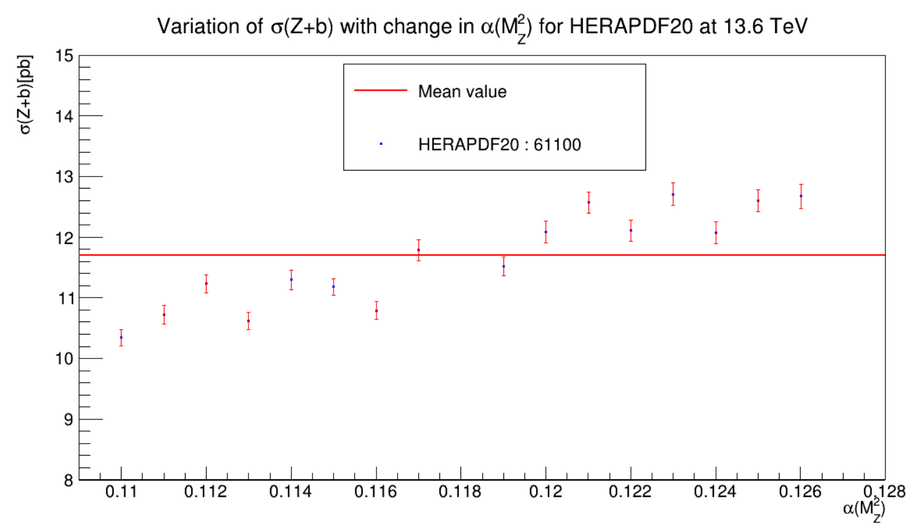

(d)

Figure 4.9: (a) shows variation in cross-section for CT10NLO, (b) shows variation in cross-section for CT14NLO , (c) shows variation in cross-section for NNPDF31NLO and (d) shows variation in cross-section for HERAPDF20 , with respect to change in choice of $\alpha_s(M_Z^2)$. The verticle bars represent PDF uncertainty and red line represents average value of cross-section for respective PDFs.

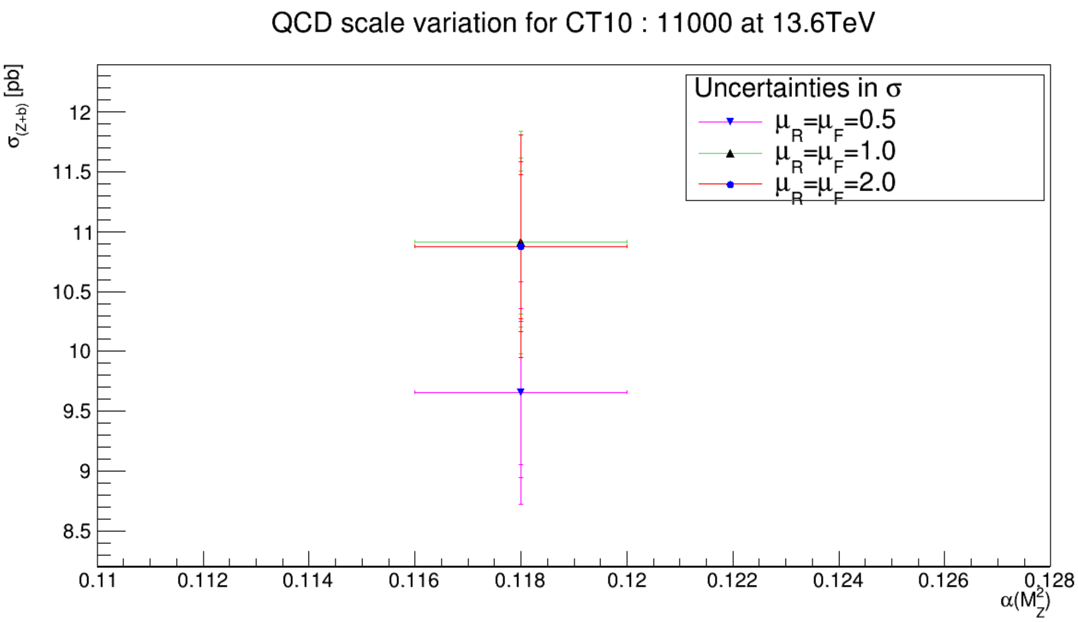
QCD scale variation for CT10 : 11000 at 13.6TeV
Uncertainties in σ
μR=μF=0.5
μR=μF=1.0
μR=μF=2.0
σ(Z+b) [pb]
α(M_Z^2)

(a)

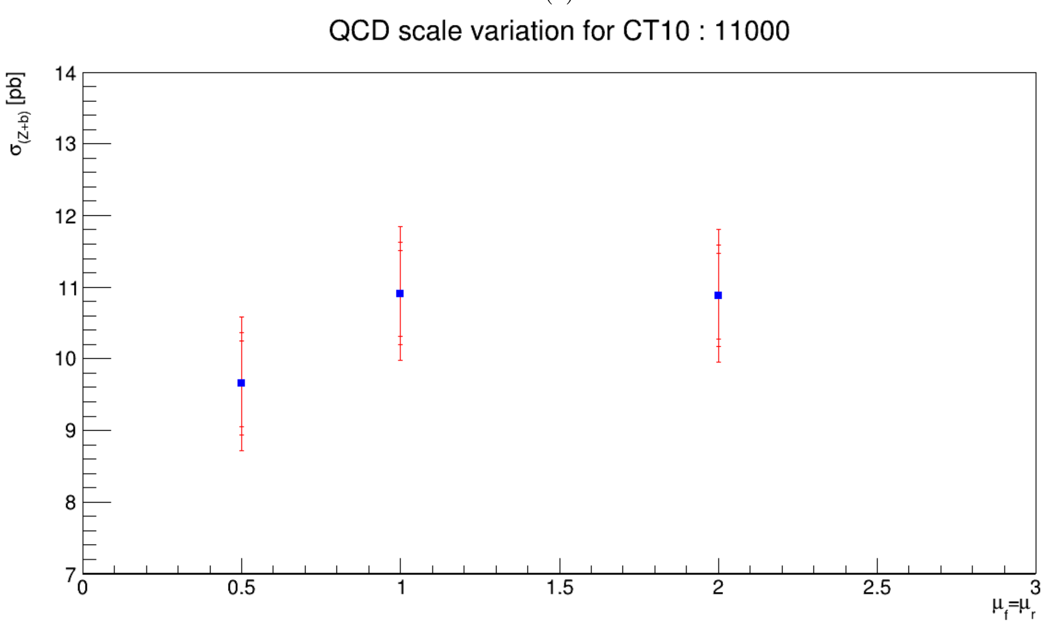
QCD scale variation for CT10 : 11000
σ(Z+b) [pb]
μf=μr

(b)

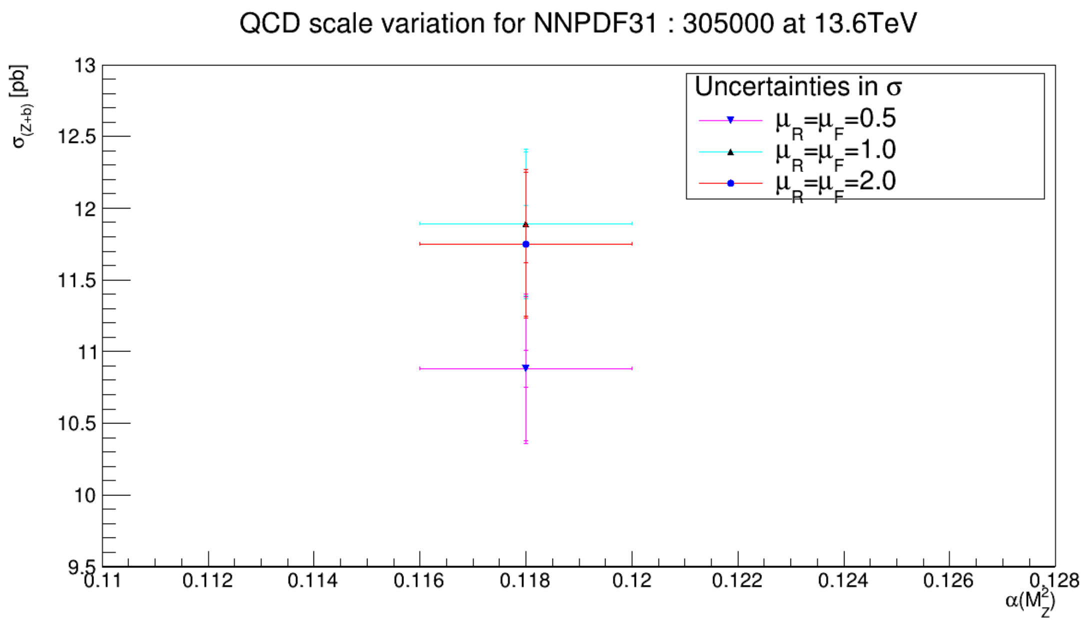

(c)

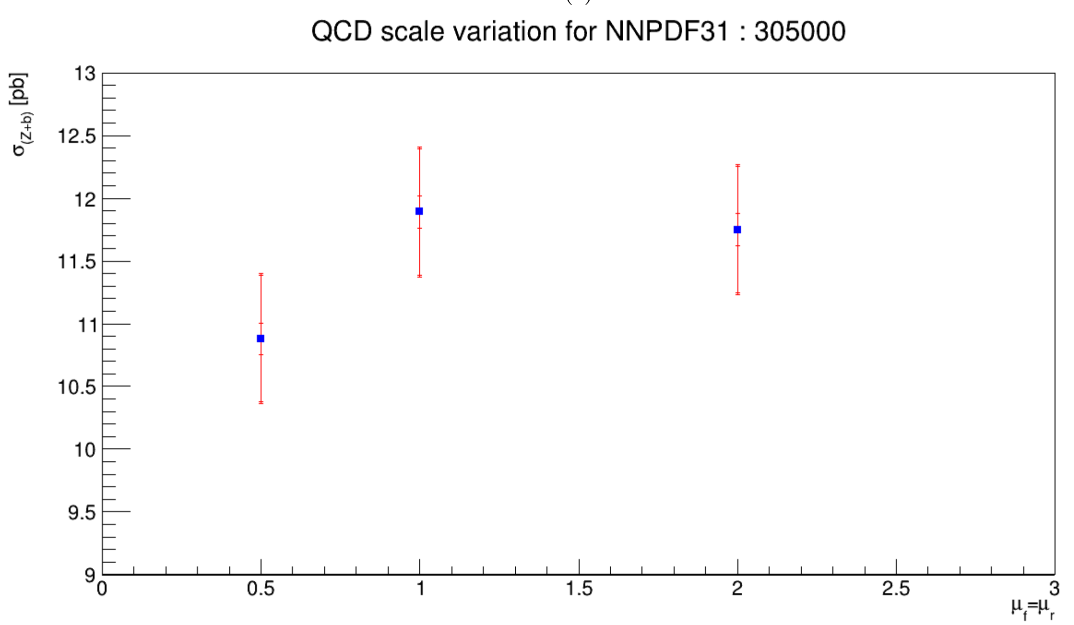

(d)

Figure 4.10: (a) and (b) shows value of cross-section at different values of QCD scales for CT10 PDF while (c) and (d) show value of cross-section at different values of QCD scales for NNPDF31 PDF. Inner bars represent pdf, middle bar represent α_s and outer bar represent pdf+α_s uncertainties.

4.5 Predictions and Uncertainties in cross-section of Z+b production at 14TeV.

4.5.0.0.1 Predicted cross section at 14TeV

The production cross-section of Z+b predicted at 14TeV of C.O.M. energy by using different PDF sets is listed below in Table 4.4 . For predictions NNPDF3.1NLO , CT10NLO , Ct14NLO , and HERAPDF20 are used.

Measured Cross-section [Pb]	PDF set	Predicted Value [Pb] (value± stat)
Not yet measured	NNPDF3.1NLO	11.89 ± 0.16
	CT10NLO	11.96 ± 0.18
	CT14NLO	11.65 ± 0.18
	HERAPDF20	11.77 ± 0.19

Table 4.4: Predicted values of X-section of Z+b production For leptonic channel of Z at 14TeV .

The results of predicted cross-section and uncertainites at 14TeV for different sets of PDF are shown in Figure 4.11 .

The variation of cross-section by changing the value of $\alpha_s(M_Z^2)$ is shown in Figure 4.12 .

Change in predicted cross-section by changing QCD scales (μ_F and μ_R) is shown in Figure 4.13 for CT10 and NNPDF31.

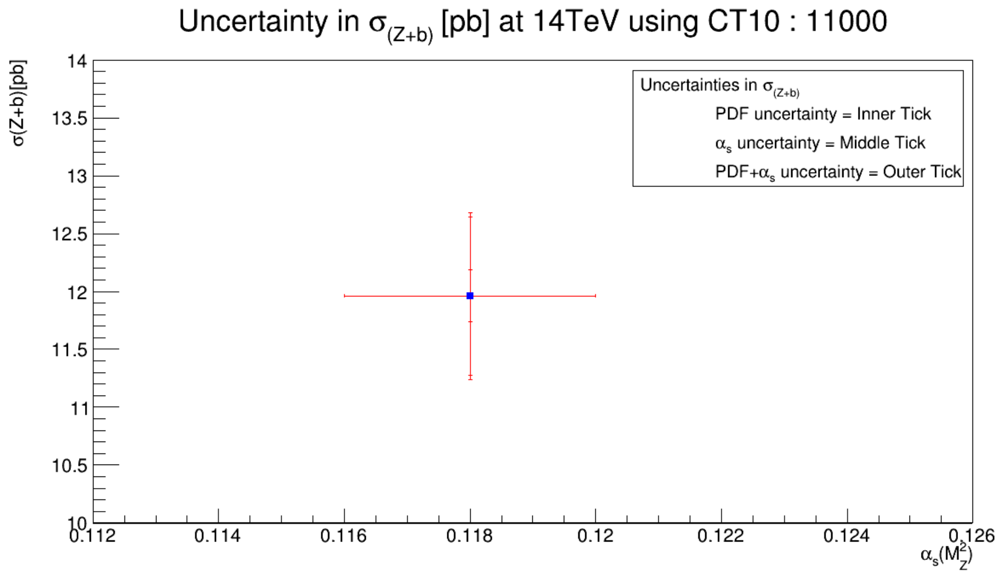

Uncertainty in σ(Z+b) [pb] at 14TeV using CT10 : 11000
σ(Z+b)[pb]
Uncertainties in σ(Z+b)
PDF uncertainty = Inner Tick
αs uncertainty = Middle Tick
PDF+αs uncertainty = Outer Tick
14
13.5
13
12.5
12
11.5
11
10.5
10
0.112
0.114
0.116
0.118
0.12
0.122
0.124
0.126
αs(M2Z)

(a)

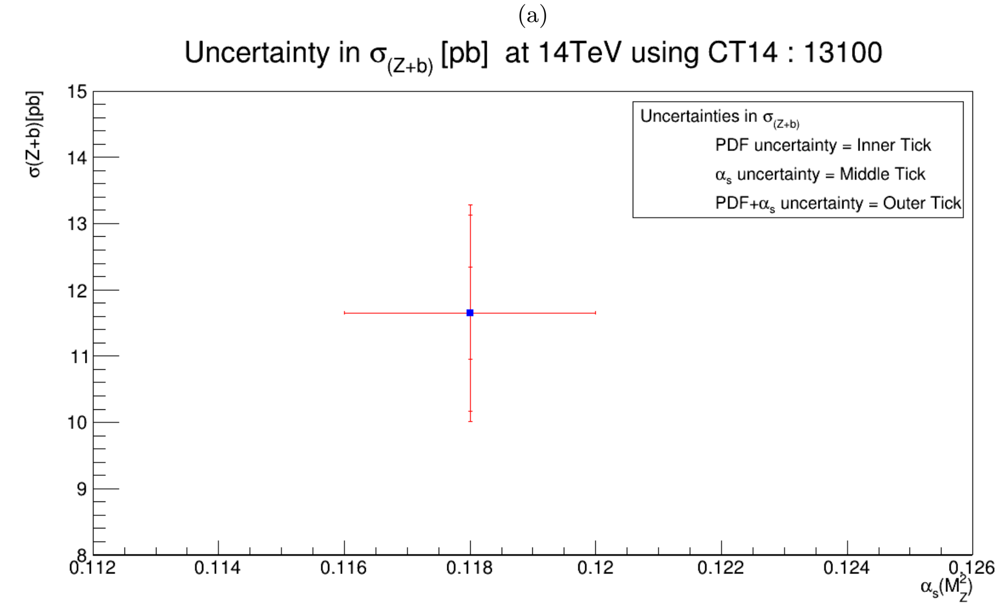

Uncertainty in σ(Z+b) [pb] at 14TeV using CT14 : 13100
σ(Z+b)[pb]
Uncertainties in σ(Z+b)
PDF uncertainty = Inner Tick
αs uncertainty = Middle Tick
PDF+αs uncertainty = Outer Tick
15
14
13
12
11
10
9
8
0.112
0.114
0.116
0.118
0.12
0.122
0.124
0.126
αs(M2Z)

(b)

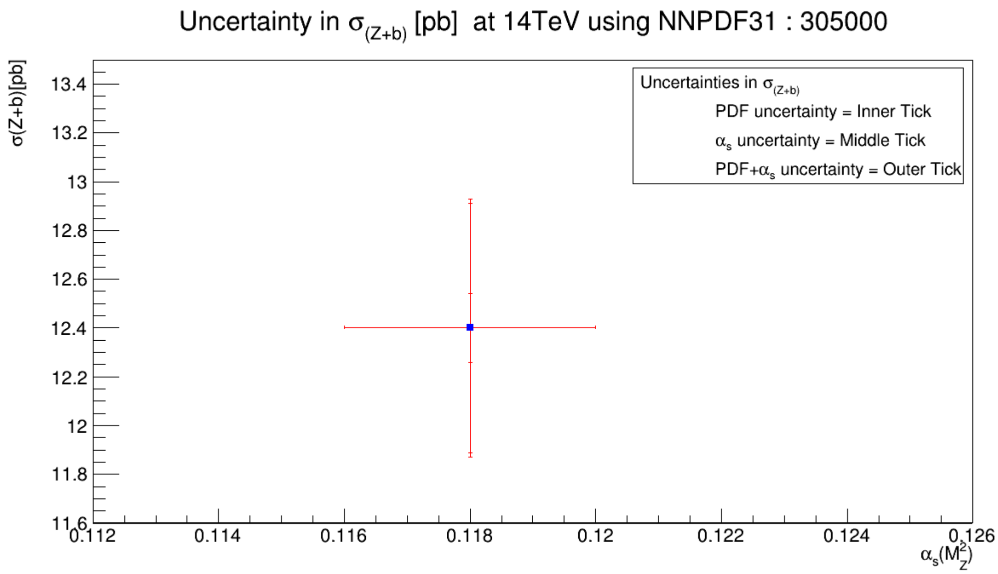

(c)

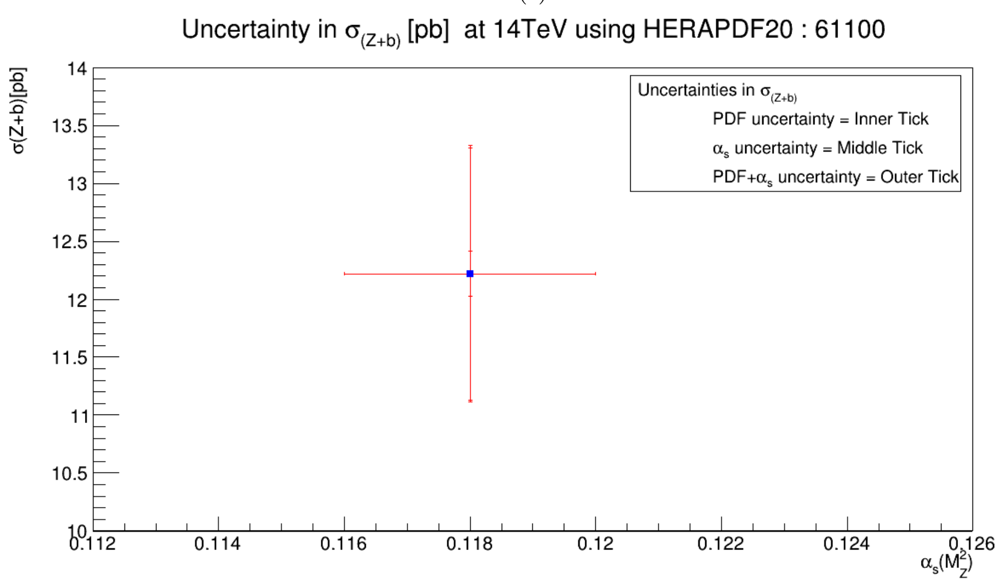

(d)

Figure 4.11: Plot (a) shows predicted cross-section and uncertainities ($pdf \pm \alpha_s \pm pdf + \alpha_s$) in cross-section by using CT10 , plot (b) shows predicted cross-section and uncertainties ($pdf \pm \alpha_s \pm pdf + \alpha_s$) in cross-section by using CT14 , plot (c) shows predicted cross-section and uncertainties ($pdf \pm \alpha_s \pm pdf + \alpha_s$) in cross-section by using NNPDF31 and plot (d) shows predicted cross-section and uncertainties ($pdf \pm \alpha_s \pm pdf + \alpha_s$) in cross-section by using HERAPDF20 .

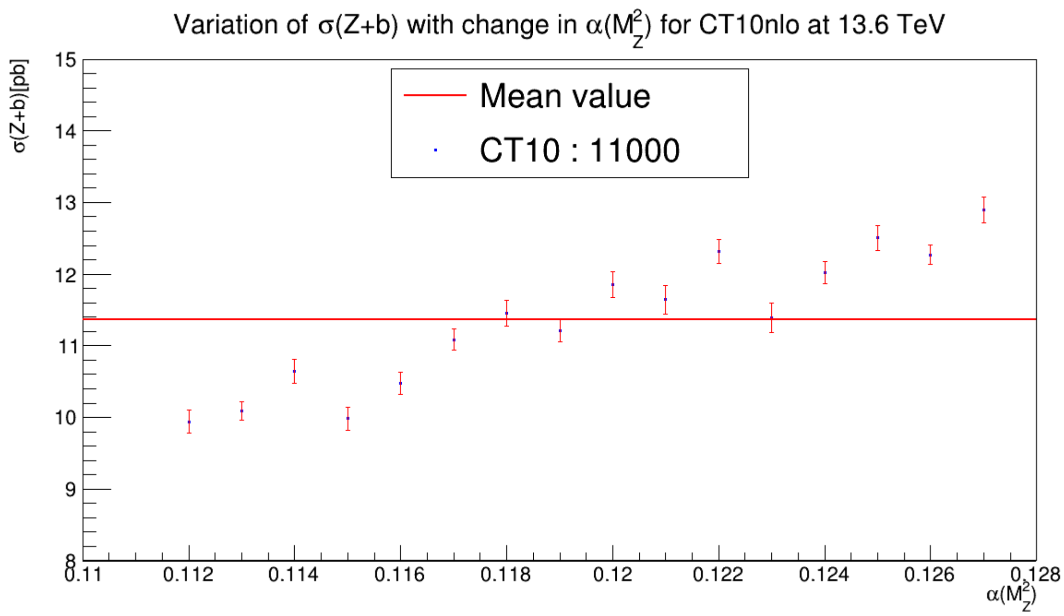

Variation of σ(Z+b) with change in α(M_Z^2) for CT10nlo at 13.6 TeV
σ(Z+b)[pb]
Mean value
CT10 : 11000
15
14
13
12
11
10
9
8
0.11
0.112
0.114
0.116
0.118
0.12
0.122
0.124
0.126
0.128
α(M_Z^2)

(a)

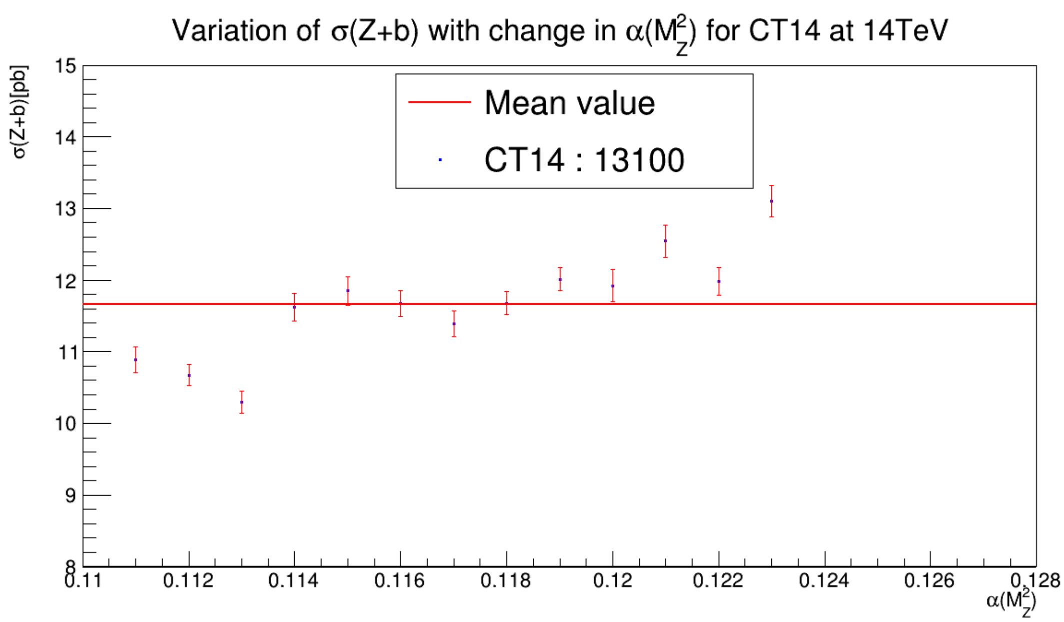

Variation of σ(Z+b) with change in α(M_Z^2) for CT14 at 14TeV
σ(Z+b)[pb]
Mean value
CT14 : 13100
15
14
13
12
11
10
9
8
0.11
0.112
0.114
0.116
0.118
0.12
0.122
0.124
0.126
0.128
α(M_Z^2)

(b)

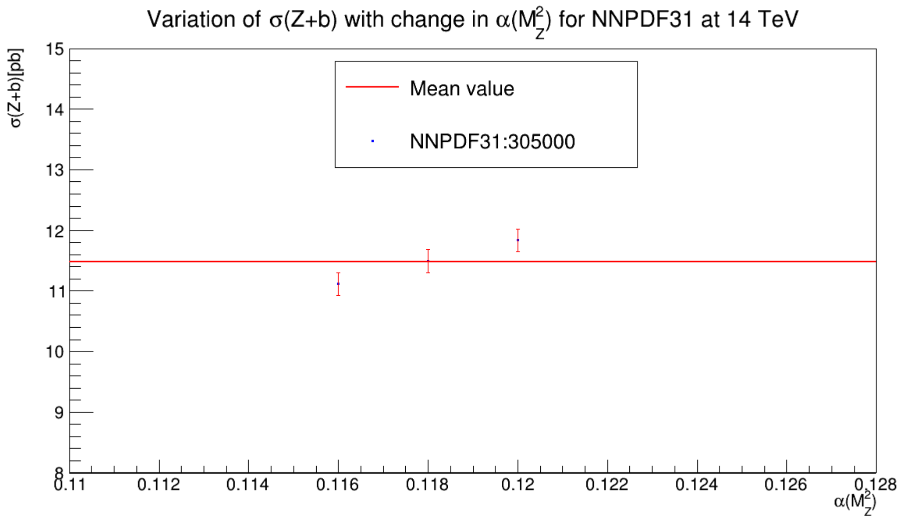

(c)

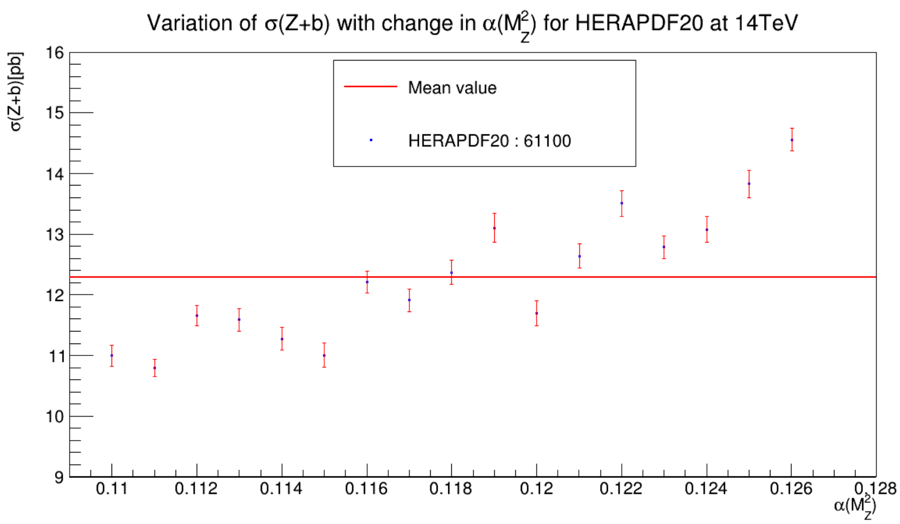

(d)

Figure 4.12: (a) shows variation in cross-section for CT10NLO, (b) shows variation in cross-section for CT14NLO , (c) shows variation in cross-section for NNPDF31NLO and (d) shows variation in cross-section for HERAPDF20 , with respect to change in choice of $\alpha_s(M_Z^2)$. The verticle bars represent PDF uncertainty and red line represents average value of cross-section for respective PDFs.

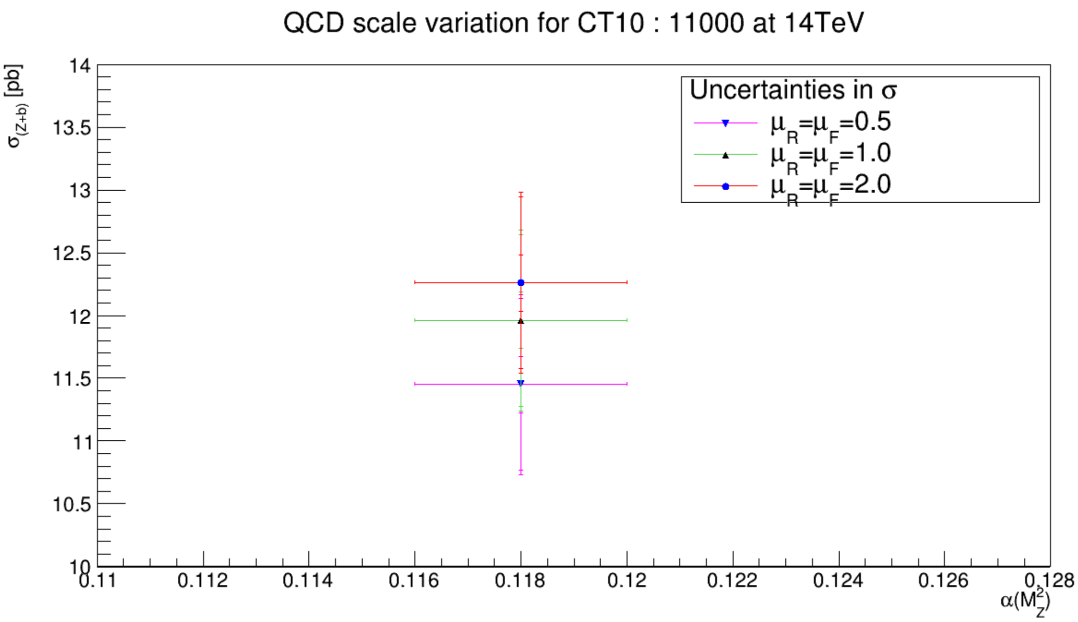
QCD scale variation for CT10 : 11000 at 14TeV
$\sigma_{(Z+b)}$ [pb]
Uncertainties in σ
$\mu_R=\mu_F=0.5$
$\mu_R=\mu_F=1.0$
$\mu_R=\mu_F=2.0$
14
13.5
13
12.5
12
11.5
11
10.5
10
0.11
0.112
0.114
0.116
0.118
0.12
0.122
0.124
0.126
0.128
$\alpha(M_Z^2)$

(a)

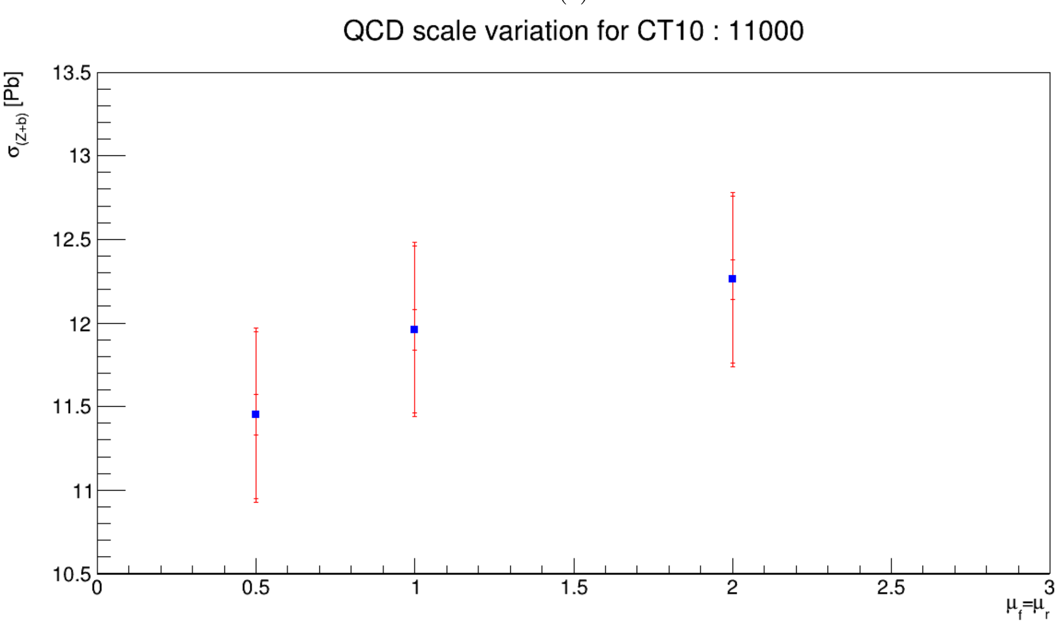
QCD scale variation for CT10 : 11000
$\sigma_{(Z+b)}$ [Pb]
13.5
13
12.5
12
11.5
11
10.5
0
0.5
1
1.5
2
2.5
3
$\mu_f=\mu_r$

(b)

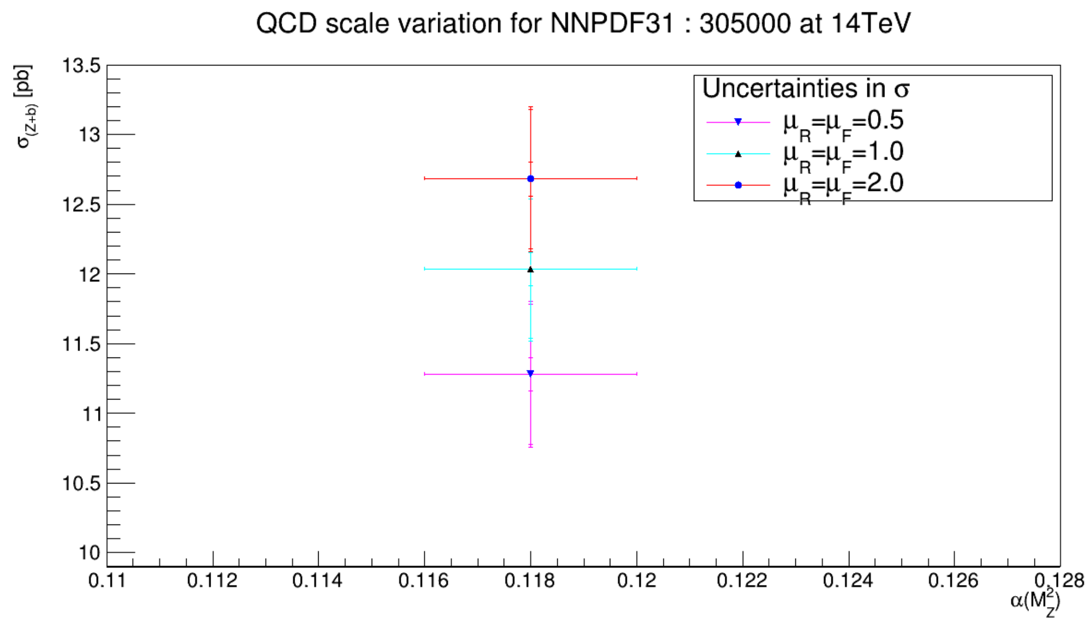

(c)

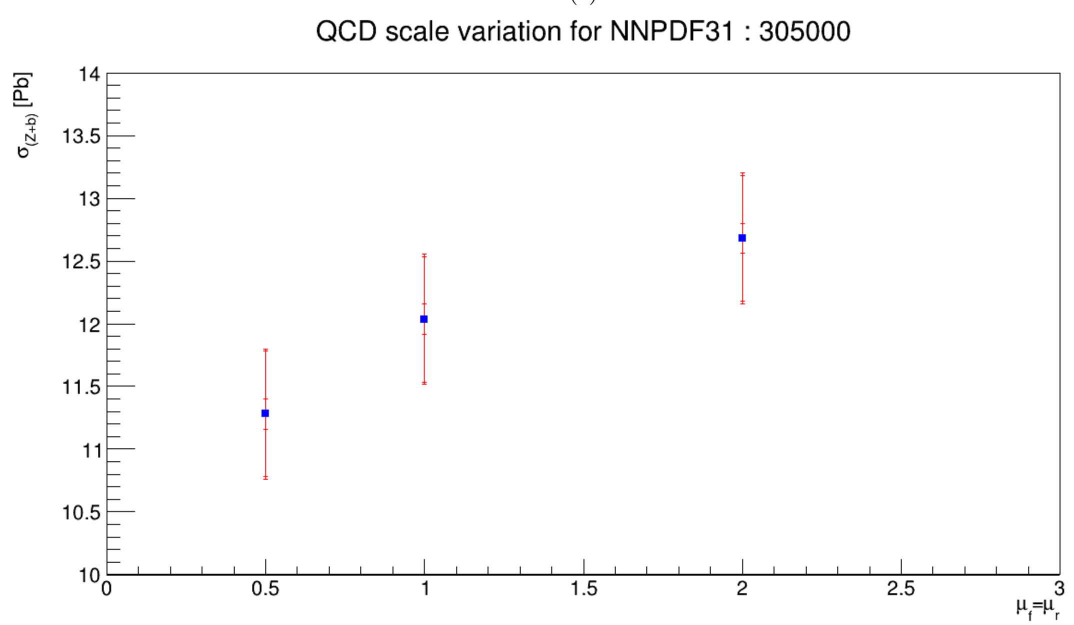

(d)

Figure 4.13: (a) and (b) shows value of cross-section at different values of QCD scales for CT10 PDF while (c) and (d) show value of cross-section at different values of QCD scales for NNPDF31 PDF. Inner bars represent pdf, middle bar represent α_s and outer bar represent pdf+α_s uncertainties.

4.6 Kinematic plots

Generator level kinematic distributions are presented in this section. The kinematics are plotted at 13TeV , 13.6TeV and 14 TeV.
Figure 4.14, Figure 4.15 and Figure 4.16 shows the transverse momentum and pseudo rapididity of *b*-quark at 13TeV ,3.6TeV and 14TeV respectively.

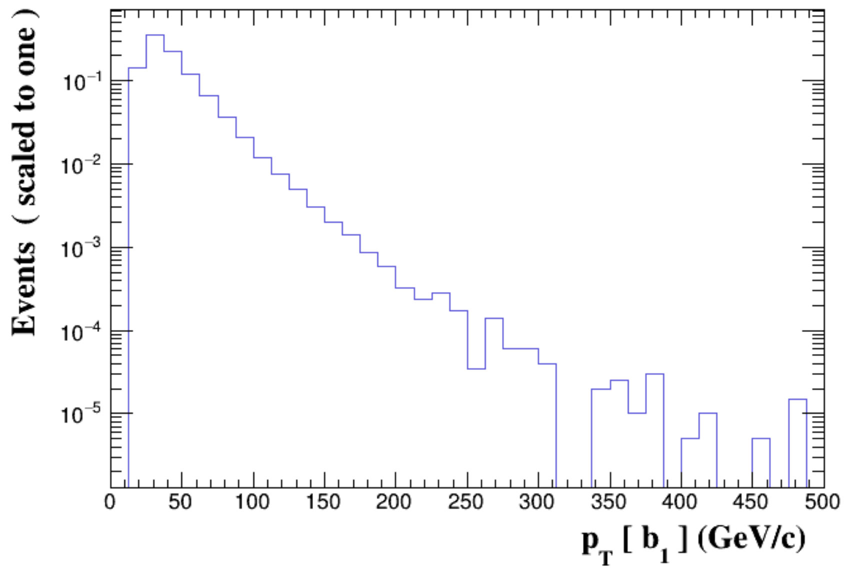

(a)

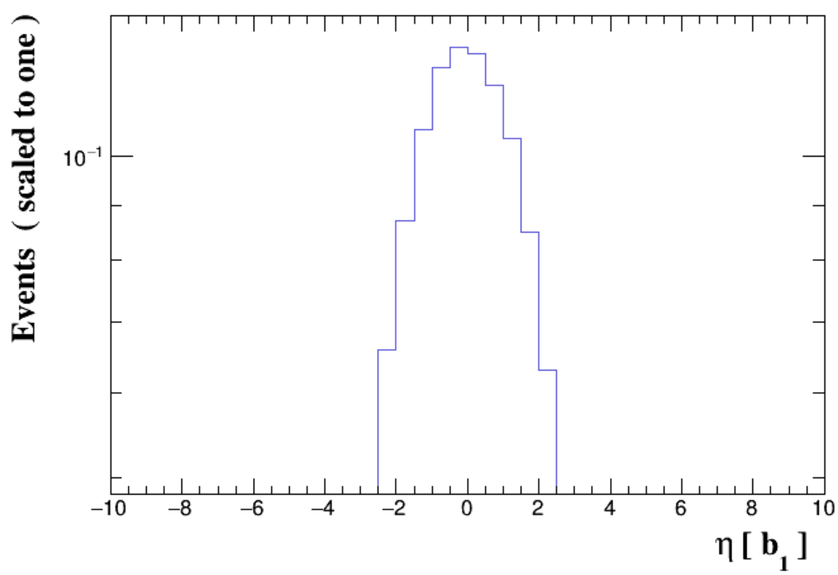

(b)

Figure 4.14: (a) shows theoretically predicted tranverse momentum distribution and (b) shows pesudo rapidivity distribution of b quark at 13TeV.

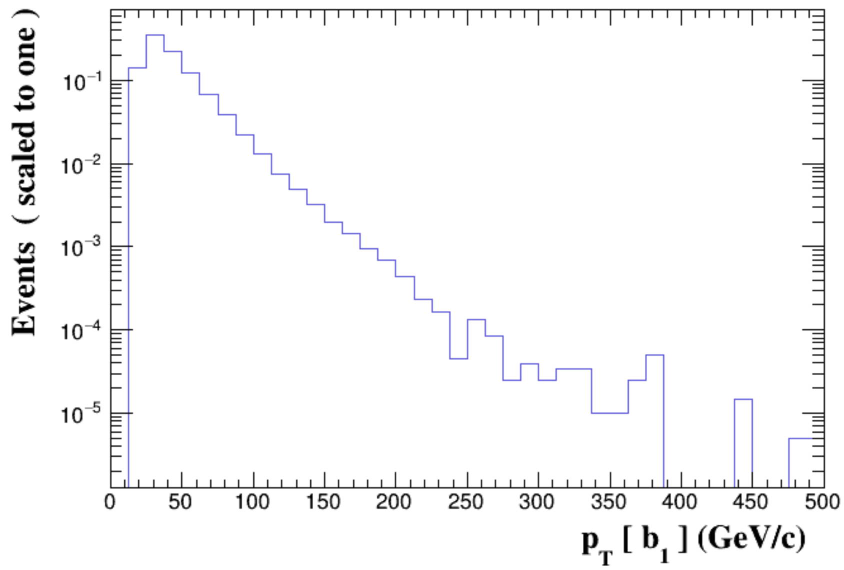

(a)

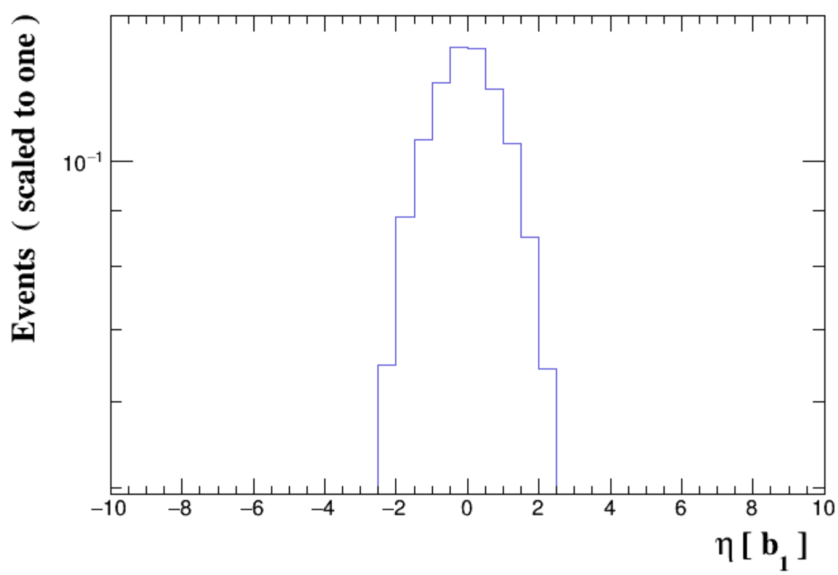

(b)

Figure 4.15: (a) shows theoretically predicted tranverse momentum distribution and (b) shows pesudo rapidivity distribution of b quark at 13.6TeV.

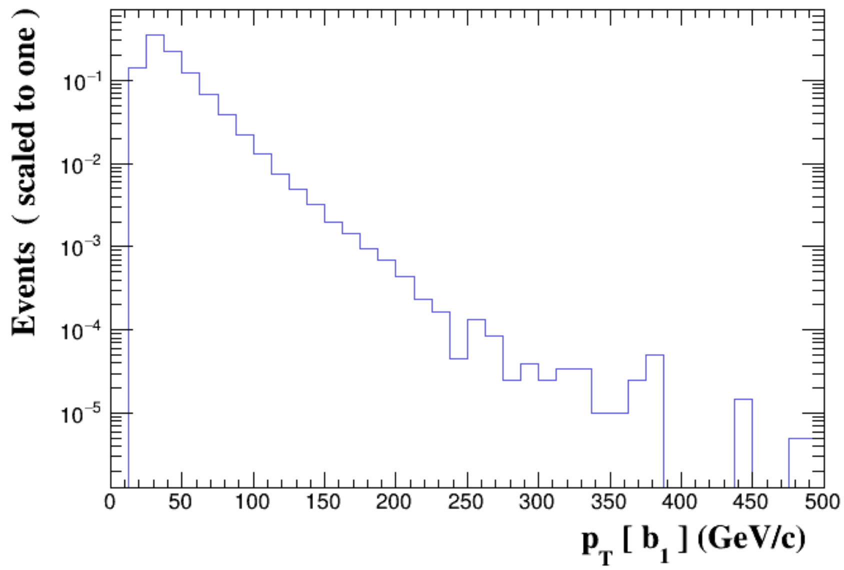

(a)

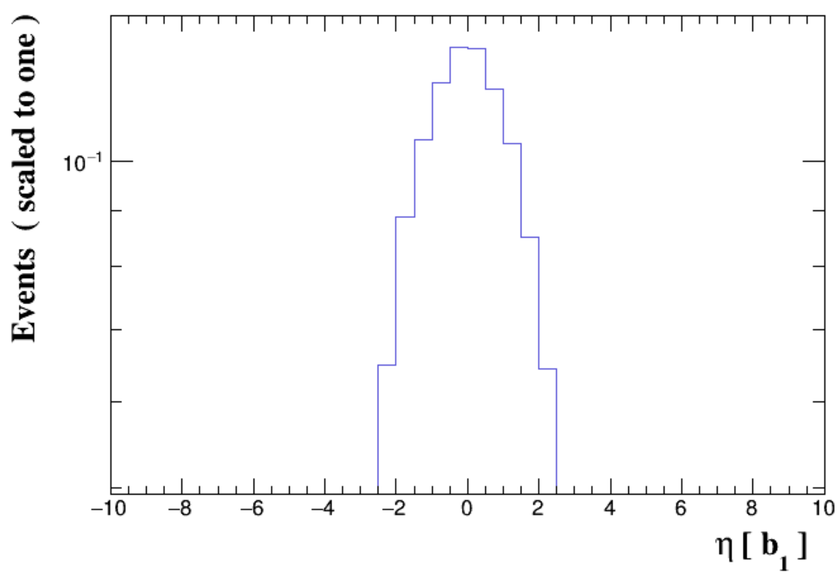

(b)

Figure 4.16: (a) shows theoretically predicted tranverse momentum distribution and (b) shows pesudo rapidivity distribution of b quark at 14TeV.

4.7 Conclusions

The study of the Z-boson and b quark production cross section is vital since $Z + b$ serve as background events for many essential processes in the Standard Model, particularly those involving the Higgs boson. Measurements of this process give the most stringent tests of perturbative quantum chromodynamics (pQCD) and are critical for a thorough understanding and modelling of QCD interactions. It also offers information about the bottom quark concentration of the proton. The great accuracy achieved in the results allows to restrict PDFs, which are the major source of uncertainty in multi-parton final state modelling, based on comparisons with theoretical predictions.

The production cross section ($\sigma_{(z+b)}$) of the Z-boson and the b quark ($Z + b$) was studied in depth in this thesis. The measured results of $Z + b$ production crossection at 7TeV with 4.6fb^{-1} of luminosity and 13TeV with 35.6fb^{-1} of luminosity are compared with the predicted cross sections. The observed and predicted cross sections show a high degree of agreement.

We also studied about various theoretical uncertainties in the predictions including PDF , α_s , QCD scale uncertainties etc. The kinematics of b quark are also shown.

We also developed theoretical predictions at various QCD scales for the $Z + b$ production cross section at 13.6TeV and 14TeV. When the data is available, these predictions will be compared to the observations. We expect the predictions for 13.6TeV and 14TeV to be comparable to the data, as they were with the previous results.

Bibliography

[1] Georges Aad et al. "Measurements of the production cross-section for a Z boson in association with b-jets in proton-proton collisions at $\sqrt{s} = 13TeV$ with the ATLAS detector". In: *Journal of High Energy Physics* 2020.7 (2020), pp. 1–58.

[2] CMS Collaboration. *The Z and B*. CMS Physics Analysis Summary. 2016-Jul-18. URL: https://cms.cern/index.php/news/z-and-b.

[3] CMS Collaboration et al. "Measurement of the production cross section for Z+ b jets in proton-proton collisions at $\sqrt{s} = 13\text{TeV}$". In: *arXiv preprint arXiv:2112.09659* (2021).

[4] Robin Devenish and Amanda Cooper-Sarkar. *31*. OUP Oxford, 2011.

[5] *HyperPhysics,Fundamental Forces, author=Nave, Rod*. Georgia State University, Department of Physics and Astronomy, 2000.

[6] "Monte carlo generators, author=Sjostrand, Torbjorn". In: *arXiv preprint hep-ph/0611247* (2006).

[7] "The PDF4LHC working group interim report, author=Alekhin, Sergey and Alioli, Simone and Ball, Richard D and Bertone, Valerio and Blumlein, Johannes and Botje, Michiel and Butterworth, Jon and Cerutti, Francesco and Cooper-Sarkar, Amanda and de Roeck, Albert and others". In: *arXiv preprint arXiv:1101.0536* (2011).

[8] "High-precision α_s measurements from LHC to FCC-ee, author=David d Enterria ". In: *arXiv preprint arXiv:1512.05194* (2015).

[9] "Renormalisation in Quantum Field Theory, author=Mukhi, Sunil". In: *arXiv preprint arXiv:1908.04075* (2019).

[10] *CMS slice image view (transverse/longitudinal/3-D), author=Davis, Siona Ruth*. Tech. rep. 2016.

[11] *Beyond The Standard Model publisher = Wikipedia contributors*.

[12] "Parton distributions for the LHC, author=Martin, Alan D and Stirling, W James and Thorne, Robert S and Watt, G". In: *The European Physical Journal C* 63.2 (2009), pp. 189–285.

[13] "Parton distributions for the LHC, author=Martin, Alan D and Stirling, W James and Thorne, Robert S and Watt, G". In: *The European Physical Journal C* 63.2 (2009), pp. 189–285.

[14] "Matching NLO QCD computations and parton shower simulations, author=Frixione, Stefano and Webber, Bryan R". In: *Journal of High Energy Physics* 2002.06 (2002), p. 029.

[15] "Introducing an innovative approach of teaching the Standard Model of particle physics at high school, author=Lindenau, Philipp and Kobel, Michael". In: IOP Publishing, 2019.

[16] "LHC machine, author=Evans, Lyndon and Bryant, Philip". In: *Journal of instrumentation* (2008).

[17] "The ALICE experiment at the CERN LHC, author=Aamodt, Kenneth and Quintana, A Abrahantes and Achenbach, R and Acounis, S and Adamová, D and Adler, C and Aggarwal, M and Agnese, F and Rinella, G Aglieri and Ahammed, Z and others, journal=Journal of Instrumentation". In: 3 ().

[18] *The ATLAS experiment at the CERN large hadron collider, author=Collaboration, ATLAS and Aad, G and Abat, E and Abdallah, J and Abdelalim, AA and Abdesselam, A and Abdinov, O and Abi, BA and Abolins, M and Abramowicz, H and others.* 2008.

[19] "The LHCb detector at the LHC, author=Alves Jr, A Augusto and Andrade Filho, LM and Barbosa, AF and Bediaga, I and Cernicchiaro, G and Guerrer, G and Lima Jr, HP and Machado, AA and Magnin, J and Marujo, F and others". In: *Journal of instrumentation* 3 (2008).

[20] "Performance of the CMS drift-tube chamber local trigger with cosmic rays, author=CMS Collaboration and others". In: *Journal of Instrumentation* 5.03 (2010), T03003.

[21] "Implications of CTEQ global analysis for collider observables, author=Nadolsky, Pavel M and Lai, Hung-Liang and Cao, Qing-Hong and Huston, Joey and Pumplin, Jon and Stump, Daniel and Tung, Wu-Ki and Yuan, C-P". In: *Physical Review D* 78.1 (2008), p. 013004.

[22] "3-, 4-, and 5-flavor next-to-next-to-leading order parton distribution functions from deep-inelastic-scattering data and at hadron colliders, author=Alekhin, S and Blümlein, J and Klein, S and Moch, S". In: *Physical Review D* 81.1 (2010), p. 014032.

[23] "Spontaneous symmetry breaking, gauge theories, the Higgs mechanism and all that, author=Bernstein, Jeremy". In: *Reviews of modern physics* 46.1 (1974), p. 7.

[24] "MadGraph 5: going beyond, author=Alwall, Johan and Herquet, Michel and Maltoni, Fabio and Mattelaer, Olivier and Stelzer, Tim". In: *Journal of High Energy Physics* 2011.6 (2011), pp. 1–40.

[25] "Measurement of differential production cross-sections for a Z boson in association with b-jets in 7 TeV proton-proton collisions with the ATLAS detector, author=Aad, Georges and Abbott, B and Abdallah, J and Abdel Khalek, S and Aben, R and Abi, B and Abolins, M and AbouZeid, OS and Abramowicz, H and Abreu, H and others". In: *Journal of High Energy Physics* 2014.10 (2014), pp. 1–49.

[26] "Review of single vector boson production in pp collisions at $\sqrt{s} = 7$ TeV, author=Schott, Matthias and Dunford, Monica". In: *The European Physical Journal C* 74.7 (2014), pp. 1–59.

[27] *Introduction to elementary particles, author=Griffiths, David*. John Wiley & Sons, October 2008.

[28] *A short journey to the infinitely small Fundamentals of Particle Physics, author=Stefania Ricciardi RAL*. March 2009.

[29] *Total Integrated Luminosity and Data Quality in 2015–2018, author=ATLAS Collaboration and others*. 2019.

[30] "Quantum Chromodynamics: High Energy Experiments and Theory, author=Dissertori, Günther and Knowles, Ian and Schmelling, Michael and Grinstein, Benjamin". In: (2004).

[31] "Fundamental interaction, author=Salam, Abdus". In: *Access Science* (2020).

[32] "Electroweak interaction , author=Baltay, Charles". In: *Access Science* (2018).

[33] *Introduction to High Energy Physics, author=Donald H. Perkins*. Cambridge University Press, June 2012.

[34] "The CMS experiment at the CERN LHC, author=Chatrchyan, S". In: *Journal of Instrumentation* 3 (2008).

[35] "The standard model: a beautiful but flawed theory, author=Gagnon, Pauline". In: *Quantum Diaries* (2015).

[36] "Evidence for $Z_0 \rightarrow$ e+ e- at the CERN pp Collider, author=Bagnaia, Po and Banner, M and Battiston, R and Bloch, Ph and Bonaudi, F and Borer, K and Borghini, M and Chollet, J-C and Clark, AG and Conta, C and others". In: *Physics Letters B* 129.1-2 (1983), pp. 130–140.

[37] "Regularization and renormalization of gauge fields, author=Veltman, Martinus and others". In: *Nuclear Physics B* (1972), pp. 189–213.

[38] "Precision NNLO determination of αs (MZ) using an unbiased global parton set, author=Ball, Richard D and Bertone, Valerio and Del Debbio, Luigi and Forte, Stefano and Guffanti, Alberto and Latorre, Jose I and Lionetti, Simone and Rojo, Juan and Ubiali, Maria and Nnpdf Collaboration and others". In: *Physics Letters B* 707.1 (2012), pp. 66–71.

[39] *An introduction to quantum field theory, author=Peskin, Michael*. CRC press, 2018.